Tectonic rotations and internal structure of Eocene plutons in Chuquicamata, northern Chile

R. Somoza [a,*], A.J. Tomlinson [b], C.B. Zaffarana [a], S.E. Singer [a], C.G. Puigdomenech Negre [a], M.I.B. Raposo [c], J.H. Dilles [d]

[a] IGEBA, CONICET-Universidad de Buenos Aires, Argentina
[b] Servicio Nacional de Geología y Minería, Santiago, Chile
[c] Instituto de Geociências, Universidade de São Paulo, Brazil
[d] Department of Geosciences, Oregon State University, Corvallis, OR, USA

ARTICLE INFO

ABSTRACT

A paleomagnetic and AMS study on Eocene plutonic complexes in the Calama area, northern Chile, reveals high-temperature, high-coercivity magnetizations of dominantly thermoremanent origin and magnetic fabrics controlled by magnetite. The paleomagnetic results indicate that ~43 Ma plutons underwent clockwise tectonic rotation, whereas adjacent ~39 Ma plutons did not undergo discernible rotation. This points to a middle Eocene age for the younger tectonic rotations associated with the Central Andean Rotation Pattern in the Chuquicamata–Calama area.

The petrofabric in these rocks formed under conditions ranging from purely magmatic (i.e. before full crystallization) to low-temperature solid-state deformation. AMS and paleomagnetism suggest that the plutonic bodies were formed by progressive amalgamation of subvertical magma sheets spanning multiple magnetic polarity chrons. The parallelism between magmatic and tectonic foliations suggests that regional tectonic stress controlled ascent, emplacement and rock deformation during cooling. In this context, we suggest that magma ascent and emplacement in the upper crust likely exploited Mesozoic structures which were locally reactivated in the Eocene.

© 2015 Elsevier B.V. All rights reserved.

1. Introduction

The Central Andean orogen (Fig. 1a) is the product of Late Cretaceous to recent magmatism and deformation driven by subduction of oceanic lithosphere beneath continental South America (Isacks, 1988; Mégard, 1984, 1987; Mpodozis and Ramos, 1990; Ramos, 1999; Ramos and Aleman, 2000). A conspicuous feature of the orogenic evolution is the persistent forelandward shift of the main magmatic and deformation loci through time.

During the Jurassic and Early Cretaceous most of the Central Andean region was close to sea level and with development of extensional basins, suggesting that slab rollback dominated the subduction zone in those times. South America began to episodically override the trench in the Late Cretaceous (Somoza and Zaffarana, 2008), leading to the first manifestations of Andean contractional deformation in Chile and Perú, which were expressed as uplift of arc massifs and tectonic inversion of the Jurassic–Early Cretaceous extensional basins (Callot et al., 2008; Charrier et al., 2007; Mamani et al., 2010; Mpodozis and Ramos,

1990). Slowdown of the westward continental motion in latest Cretaceous likely produced a renewed predominance of slab rollback over trench overriding (Somoza and Zaffarana, 2008), leading to the development of fault-bounded basins in northern Chile (Cornejo et al., 2003) which in turn were inverted around the Cretaceous–Cenozoic boundary as the product of a renewed contractional deformation (Cornejo et al., 2003; Somoza et al., 2012). Neutral to slightly extensional conditions continued through the Paleocene till the middle to late Eocene, when the widespread Incaic contractional phase occurred along a great extent of the Andean margin. Farther east, the Eastern Cordillera of Bolivia begun to form early in the Oligocene (Hongn et al., 2007; Lamb and Hoke, 1997; McQarrie et al., 2005; McQuarrie, 2002), leading to isolation of the area currently occupied by the Altiplano as an internally drained basin with sediment supply from uplifted areas in its eastern and western sides. From late Oligocene to late Miocene the main deformation occurred in the Altiplano–Puna region and possibly the Eastern Cordillera (e.g. Lamb and Hoke, 1997), and since the late Miocene the main locus of shortening passed to the Subandean fold-thrust belt, with most of the previously deformed areas converging passively toward the craton.

A first order feature of the Central Andean deformation is the presence of a pattern of vertical-axis rotations, clockwise in the southern branch of the orogen and anticlockwise in its northern branch

* Corresponding auhtor at: Departamento de Ciencias Geológicas, Pabellón 2, Ciudad Universitaria, Buenos Aires, C1428EHA, Argentina.
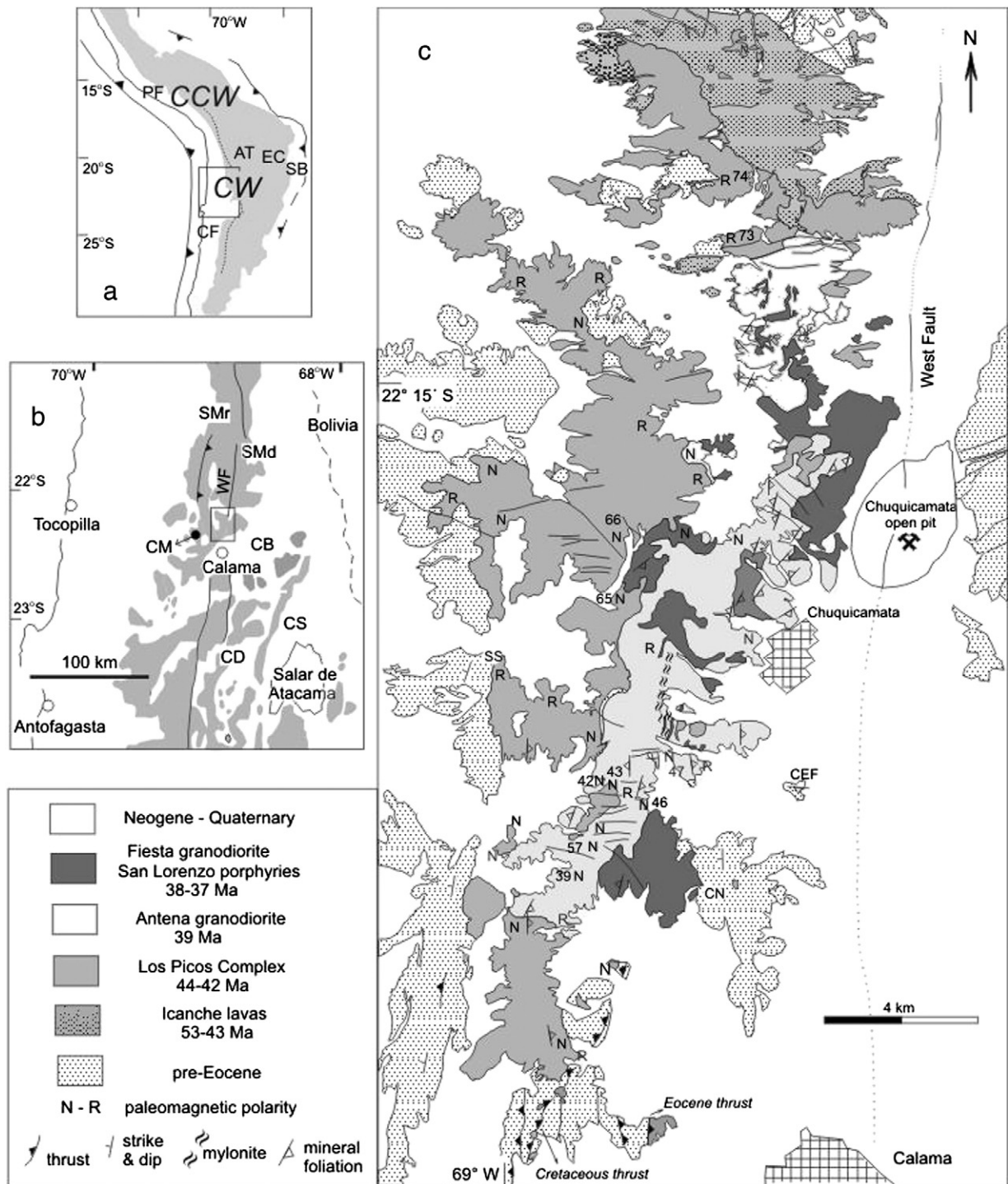E-mail address: somoza@gl.fcen.uba.ar (R. Somoza).

Fig. 1. a) General view of the Central Andean megasalient. Gray encloses the area above 3 km topography (Isacks, 1988). CW and CCW denote the clockwise and counterclockwise domains of the Central Andean Rotation Pattern (CARP, see main text). PF and CF are Peruvian and Chilean margins, AT, EC and SB are Altiplano, Eastern Cordillera and Subandean Belt, respectively. Box denotes the area in Fig. 1b. b) Outcrops of the Precordillera of northern Chile. Codes denote main morphotectonic units: Sierra de Moreno (SMr); Sierra del Medio (SMd); Calama Basin (CB); Cerros de Montecristo (CM; black dot); West Fault (WF); Cordillera de Domeyko (CD); Cordillera de la Sal (CS). Box indicates the study area (Fig. 1c); c) Eocene igneous rocks near Chuquicamata. Map shows the main structural elements. Sites with positive paleomagnetic results are shown indicating the observed magnetic polarity (N–R for normal and reversed, respectively). Numbers identify pairs of neighbor sites sharing similar paleomagnetic direction: FC39–FC57; FC42–FC43; FC46–FC47; LP65–LP66; LP73–LP74 (see also Table 1 and main text for discussion). The locations of Cerro Negro (CN) and the host-rock sites SS and CEF are also shown.

(Fig. 1a). Somoza et al. (1996) coined the term Central Andean Rotation Pattern (CARP) to refer to this spatial distribution of tectonic rotations. Our understanding of the spatial distribution and timing of the CARP has improved in recent years (e.g. Arriagada et al., 2000, 2003; Randall et al., 1996, 2001; Roperch et al., 2000, 2006, 2011; Rousse et al., 2003; Somoza and Tomlinson, 2002; Somoza et al., 1999; Taylor et al., 2007). In particular, the timing of rotations in northern Chile has been constrained by Somoza and Tomlinson (2002), who showed the presence of unrotated lower Miocene strata that unconformably lie on rotated Cretaceous rocks. The new paleomagnetic data reported in this paper

further refine this determination, indicating that ca 43 Ma plutons in the area of Chuquicamata underwent clockwise tectonic rotation, in agreement with the CARP, whereas ca 39 Ma plutons that intruded the former are not rotated. This constrains the younger record of the CARP in the study area to be middle Eocene, and thus to be unambiguously associated with the Incaic deformation event.

On the other hand, the sampled rocks are part of the Eocene calc-alkaline magmatism at latitudes of northern Chile and were emplaced during an important contractional event in the Central Andean evolution. This offers the possibility to explore the emplacement of magmas in the upper crust during regional shortening. We determined the magnetic fabric from these plutons in order to gain insights into their internal structure, which in turn allows inferring about their mode of emplacement.

2. The Los Picos (LPPC) and Fortuna (FPC) plutonic complexes: geology and sampling

The Precordillera of northern Chile (Fig. 1b) is a major morphotectonic unit that was the locus of an Eocene tectono-magmatic episode involving contractional deformation and arc magmatism (Mpodozis and Ramos, 1990; Reutter et al., 1996; Tomlinson et al., 2001). Around Chuquicamata (Fig. 1c), the Eocene magmatic activity is mainly represented by two adjacent, shallowly emplaced plutonic complexes of slightly differing age. Isotopic ages from these plutonic complexes (see below) indicate that they were emplaced between ca 44 and 37 Ma, constituting then the magmatic record closely associated with the Incaic contractional phase, which in the area spanned 43–35 Ma (Tomlinson et al., 2001).

The older plutonic suite is represented by the Los Picos plutonic complex (LPPC), which has 45 to 42 Ma (middle Eocene) U–Pb zircon ages (Campbell et al., 2006; Tomlinson et al., 2010). The LPPC intrudes Jurassic and Lower Cretaceous sedimentary rocks, Upper Cretaceous volcanic and volcaniclastic rocks, and 53–43 Ma andesitic lavas, the latter being penecontemporaneous lavas and therefore indicating a very shallow emplacement level for the north end of the complex (Fig. 1c). Field observations of scarce well-defined internal contacts and variations in composition and texture indicate that the Los Picos unit is essentially a composite body formed of numerous dioritic to quartz monzodioritic and quartz monzonitic intrusions, with minor quartz diorite and monzodiorite. The dominant composition of these rocks is characterized by abundant K-feldspar, <20% quartz, and clinopyroxene and biotite as the dominant mafic minerals. Propylitic alteration is present in some sites, where mafic minerals have been replaced by chlorites, epidote and titanite, and feldspars are moderately altered to sericite and clays.

The younger plutonic suite constitutes the Fortuna plutonic complex (FPC; Dilles et al., 1997, 2011), which consists of an early, large intrusion, called the Antena granodiorite, a younger, more central intrusion called the Fiesta granodiorite, and granodioritic porphyries genetically related to the Fiesta unit. The Antena plutonic body is mostly a fine- to medium-grained, amphibole-biotite granodiorite, with minor quartz-diorite and quartz monzodiorite. Field mapping in the northern sector suggests that this part of the plutonic body is composed of a series of intrusions with mostly NNE, steeply dipping contacts (Tomlinson et al., 2001). This unit yielded U–Pb zircon ages of ca 39 Ma (Campbell et al., 2006; Dilles et al., 1997). The Fiesta granodiorite (ca. 38–37 Ma, U–Pb zircon) and related porphyries form several bodies intruding the Antena unit; the porphyries having hydrothermal alteration and copper mineralization associated with them (Dilles et al., 1997, 2011).

In the southern sector of the study area (Fig. 1c), the LPPC cut east-vergent thrusts of likely Late Cretaceous age. Farther east the LPPC forms the hanging-wall block of a west-verging reverse fault, likely related to the Eocene Incaic deformation. Other mesoscale structures mapped in the LPPC and FPC correspond to E–W faults with minor displacement (Fig. 1c), some of which show dextral displacement. In the

center of the FPC, just west of Chuquicamata (Fig. 1c), there is a N–S stripe of steeply dipping mylonites with near down-dip lineations (Fig. 1c).

Information about the internal structure of these plutons is scarce and largely confined to detailed mapping in the northern half of the FPC (Fig. 1c). We applied anisotropy of low field induced magnetic susceptibility (AMS; Borradaile and Henry, 1997; Bouchez, 1997) with the aim of improving our current understanding of the internal structure of the LPPC and the Antena granodiorite, the subunit of the FPC showing the largest exposures.

This study involves 516 samples distributed in 95 sites (Table 1). Sampling was performed in order to satisfy the minimum requirements for within-site paleomagnetic statistics and provide a spatial coverage sufficient to obtain a view of the internal structure of the units. A typical site in this study consists of 4 to 7 samples distributed over an outcrop area of 100 to 500 m^2. Although some areas remain unsampled because of access difficulties, we consider that the sampling coverage is sufficient to obtain suitable AMS information. Site SSLP (Table 1; Fig. 1c) corresponds to tilted (60° to the 55° W) Jurassic–Lower Cretaceous rocks in contact with the western outcrops of the LPPC. Site CEF (Table 1; Fig. 1c) corresponds to Upper Cretaceous volcaniclastic rocks thermally metamorphosed by intrusion of the Fiesta granodiorite. The geographical coordinates of sampling locations are given in Table 1.

3. Methodology

A complete description of deformation requires information on translation, rotation, distortion and dilation. Paleomagnetism is an irreplaceable tool as the ancient Earth's magnetic field provides a reference frame in which the paleomagnetic vector quantifies the finite rigid-body rotation of rocks about any axes except those that are close to the paleomagnetic vector itself. In particular, paleomagnetism is an indispensable tool for detecting rotation of rocks about a vertical-axis. Paleomagnetic specimens from all samples in this study were subjected to progressive thermal and/or alternating field (AF) demagnetization. Paleomagnetic routines used a 2G three axes cryogenic magnetometer with a static alternating field (AF) demagnetizer attached to the magnetometer. Thermal demagnetization used an ASC Scientific oven. Paleomagnetic vectors were defined using principal component analysis (Kirschvink, 1980), and the accepted vectors usually show a maximum angular deviation (MAD) < 10°. Paleomagnetic results are listed in Table 1. The results were compared with the cratonic reference field for the Eocene determined in Somoza (2007). Rotations, inclination flattening and their confidence intervals were calculated in direction space according to Demarest (1983).

The bulk magnetic mineralogy of selected samples was explored by observing both hysteresis loops and acquisition of isothermal remanent magnetization (IRM) which were obtained using a Molspin vibrating sample magnetometer. Saturation magnetization (J_S), saturation remanence (J_R) and coercivity (H_C) were determined from hysteresis loops (induction up to 1 T), whereas coercivity of remanence (H_{CR}) was obtained after back field of IRM acquired at 0.7 T. The remanent coercivity spectra from anhysteretic remanence were determined using a partial anhysteretic remanence (pARM) magnetization procedure (Jackson et al., 1988).

Anisotropy of magnetic susceptibility (AMS) constitutes a powerful tool for investigating the internal structure of plutons by determining the preferred orientation of rock-forming minerals (e.g. Borradaile and Henry, 1997; Bouchez, 1997). AMS determines the mean preferred orientation of minerals weighted by their bulk susceptibility and by their mineral anisotropy (e.g. Borradaile, 1987). Anisotropy of low field induced magnetic susceptibility measurements in this study used a Kappabridge KLY-3S instrument. Anisotropy of remanent magnetization (Jackson, 1991), in turn, allows determine the mean preferred orientation of ferromagnetic grains in a rock. We apply anhysteretic

Table 1
Anisotropy of Low-field magnetic susceptibility and paleomagnetic results.

Los Picos complex

Site	Lat. (°S)	Long. (°W)	N/n	K$_m$ (10^{-3}SI)	Mean AMS parameters				Mean AMS eigenvectors						Mt	Paleomagnetism					
					L	F	P	T	K$_{max}$		K$_{int}$		K$_{min}$			Site	n	Decl	Incl	α$_{95}$	k
									Dec/Inc	e/z	Dec/Inc	e/z	Dec/Inc	e/z							
LP03A	22.317	68.983	6/6	28	1.011	1.009	1.020	−0.152	188/68	10/7	34/20	15/10	301/9	15/7	1						
LP06	22.317	68.983	3/3	32	1.016	1.033	1.049	0.325	27/67	38/8	237/20	37/12	143/11	13/10	3 + 4						
LP12	22.255	68.948	4/3	41	1.013	1.046	1.060	0.545	169/26	11/2	51/43	12/5	279/36	8/2							
LP12A	22.265	68.962	5/5	30	1.010	1.013	1.023	0.135	319/31	18/13	89/46	28/11	211/27	29/13	3 + 4	LP12A	5	164.8	33.8	8.5	115
LP13	22.373	68.999	6/6	43	1.029	1.021	1.051	−0.149	43/77	6/3	183/10	12/5	274/8	12/2		LP13	5	28.2	−54.6	5.0	238
LP15	22.336	68.991	12/12	51	1.028	1.025	1.054	−0.077	23/32	5/1	164/51	8/4	280/20	8/1	3 + 4						
LP17	22.326	68.986	7/7	42	1.022	1.032	1.054	0.088	37/65	21/5	189/22	20/8	283/11	9/6	2 + 3	LP17	5	220.6	43.2	14.4	21
LP19	22.410	68.985	5/5	26	1.013	1.025	1.038	0.354	99/85	10/4	8/0	10/4	278/5	6/1	3	LP19	5	215.9	44.5	12.7	28
LP20	22.398	68.986	6/6	36	1.012	1.037	1.049	0.496	94/77	42/5	341/5	42/3	250/12	7/4							
LP21	22.396	68.990	6/6	38	1.012	1.026	1.038	0.216	316/83	24/13	182/5	38/26	92/5	38/10	1						
LP22	22.403	68.984	6/7	30	1.026	1.030	1.057	0.075	25/74	8/4	179/14	11/6	271/7	10/2	3 + 4	LP22	7	15.9	−64.4	5.6	115
LP23	22.393	68.990	6/6	44	1.029	1.027	1.056	−0.106	61/72	12/7	312/6	11/10	220/17	11/7							
LP24	22.376	68.996	4/4	36	1.049	1.195	1.253	0.577	66/36	11/0	175/24	12/3	291/44	4/1	2						
LP25	22.408	69.009	7/7	36	1.010	1.009	1.019	0.055	245/12	9/4	128/65	15/8	340/22	15/6	1						
LP27	22.376	68.994	4/4	26	1.032	1.081	1.115	0.427	77/56	8/6	184/11	8/5	280/32	7/4							
LP28	22.377	68.994	4/4	26	1.044	1.215	1.269	0.636	32/61	24/3	171/23	24/3	268/17	5/2	3 + 4						
LP32	22.368	68.997	4/4	40	1.022	1.024	1.046	0.065	88/77	7/1	188/2	14/1	278/13	15/6							
LP33	22.322	68.988	4/4	21	1.016	1.037	1.053	0.375	31/9	15/8	170/78	18/12	300/8	18/9	2						
LP35[a]	22.354	68.998	6/6	34	1.026	1.059	1.087	0.390	197/8	90/8	87/66	90/12	290/22	14/8	1	LP35	6	20.7	−52.1	3.5	357
LP36	22.359	69.002	7/5	30	1.022	1.025	1.047	0.026	204/54	20/6	331/23	19/5	72/26	12/7	1	LP36	4	0.8	−61	3.6	476
LP40	22.387	68.972	9/9	48	1.018	1.016	1.034	−0.051	72/50	11/3	199/26	14/10	303/27	14/5	3 + 4	LP40	6	334.1	−51.3	7.5	81
LP44	22.340	68.980	7/7	28	1.018	1.039	1.058	0.346	36/74	11/5	203/15	12/6	294/3	8/5		LP44	5	18.3	−57.4	12	60
LP62	22.315	69.003	5/5	33	1.014	1.013	1.027	−0.024	340/1	31/15	78/80	28/16	250/10	37/19	1	LP62	5	195	32.6	10.7	52
LP63	22.282	68.997	4/4	25	1.016	1.013	1.029	−0.062	258/55	14/4	89/35	17/13	355/5	16/3	1	LP63	4	15.8	−50	7.3	125
LP64	22.281	68.996	9/9	24	1.016	1.013	1.029	−0.047	272/1	14/4	5/66	14/11	181/24	11/5	1	LP64	6	23.3	−41.7	7.8	139
LP65	22.301	68.973	4/4	56	1.010	1.032	1.043	0.523	149/44	90/7	14/36	90/12	265/24	12/6	1	LP65[c1]	4	350.5	−43.4	10.2	62
LP66	22.285	68.968	5/4	34	1.012	1.025	1.037	0.386	313/20	66/9	170/66	77/16	48/14	23/8	3	LP66[c1]	5	355.5	−45.9	5.5	320
LP69	22.197	68.995	4/4	12	1.006	1.027	1.032	0.627	309/22	90/8	41/7	90/9	148/67	8/7	3						
LP70	22.244	68.984	5/5	25	1.008	1.021	1.029	0.435	314/4	27/6	214/67	27/4	46/22	6/4	1						
LP71	22.233	68.995	4/4	26	1.019	1.039	1.059	0.345	312/73	50/10	135/17	59/9	44/1	12/7	4						
LP72	22.211	69.000	4/4	21	1.007	1.007	1.013	−0.071	91/62	13/6	237/24	31/11	334/14	30/8	4	LP72[c]	2	175.3	42.1	–	–
LP73	22.198	68.935	5/5	29	1.019	1.018	1.037	−0.039	28/78	11/5	187/11	16/11	278/4	16/6	4	LP73[c2]	5	177.9	56.8	7.6	101
LP74	22.192	68.938	4/4	37	1.008	1.027	1.034	0.573	3/45	30/8	140/36	32/17	248/23	23/7	3	LP74[c2]	4	189.4	58.4	8.1	233
LP75	22.273	68.948	4/4	41	1.023	1.074	1.098	0.508	161/9	19/2	56/59	19/6	256/30	6/4		LP75	4	179.4	55.1	18.2	23
LP77	22.240	68.952	5/5	47	1.007	1.028	1.035	0.623	68/49	90/19	332/5	90/35	238/41	32/11	2						
LP78	22.231	68.980	5/5	30	1.014	1.017	1.031	0.110	68/71	19/19	169/4	90/19	260/18	20/16	1	LP78	4	1.1	−42.9	5.1	327
LP79	22.211	68.970	4/4	36	1.010	1.018	1.028	0.262	204/77	46/13	100/3	40/32	10/13	36/21	1	LP79[a]	4	190.9	29.1	5.6	70
LP84	22.272	68.015	6/6	12	1.011	1.013	1.024	0.058	65/26	10/8	194/52	23/10	321/26	23/7		LP84	4	188.8	48.8	12.0	85
LP85	22.277	69.000	4/4	26	1.011	1.016	1.027	0.198	169/10	15/15	330/80	32/12	78/3	31/13							
LP86	22.291	68.996	4/4	20	1.013	1.012	1.024	−0.048	271/22	14/6	21/40	17/10	159/42	16/5							
LP87	22.148	68.935	6/6	32	1.008	1.013	1.021	0.172	118/67	12/7	314/22	16/7	221/6	19/8		LP87	5	24.4	−48.7	9.4	67
SSLP[a]	22.315	69.003	11	0.1	No consistent results											SSLP-N	5	12.5	−44.8	6.3	149
																SSLP-R	6	201.3	44.7	10.0	46
Mean			**42**	**32**												**LPPC**	**21**	**192.0**	**48.9**	**5.6**	**33**
																LP north	**7**	**182.1**	**45.2**	**10.5**	**34**
																LP south	**14**	**197.4**	**50.4**	**6.5**	**38**

Site	Lat. (°S)	Long. (°W)	N/n	K_m (10⁻³SI)	L	F	P	T	K_{max} Dec/Inc	e/z	K_{int} Dec/Inc	e/z	K_{min} Dec/Inc	e/z	Mt	Site	n	Decl	Incl	α95	k
					Mean AMS parameters				Mean eigenvectors							Paleomagnetism					
Antena Granodiorite																					
FC03	22.333	68.967	5/5	38	1.106	1.160	1.282	0.162	89/46	11/2	179/0	11/3	270/44	3/2							
FC04	22.333	68.950	7/7	24	1.144	1.128	1.291	−0.032	16/20	61/7	191/70	62/5	285/2	10/5	4						
FC05	22.333	68.953	5/5	42	1.052	1.087	1.143	0.265	21/19	53/7	181/70	56/9	287/6	13/6	2						
FC09[b]	22.250	68.941	6/5	38	1.048	1.048	1.098	0.014	169/13	9/4	51/64	9/6	264/23	7/5							
FC10A	22.223	68.942	4/4	44	No consistent results																
FC14	22.353	68.985	4/4	38	1.026	1.079	1.107	0.507	25/53	52/6	176/43	52/5	280/15	8/3	3						
FC16	22.347	68.980	5/4	32	1.027	1.061	1.090	0.389	26/37	30/4	205/53	30/3	296/0	4/3	2						
FC18	22.333	68.953	6/6	28	1.035	1.038	1.075	0.041	235/14	4/2	3/68	9/3	141/17	9/3	4						
FC26	22.375	68.994	8/8	27	1.032	1.038	1.071	0.079	118/62	6/4	12/8	10/5	277/26	10/3	1						
FC29	22.374	68.990	10/9	30	1.037	1.055	1.094	0.161	18/68	6/13	195/22	7/5	286/1	7/3	3						
FC31	22.370	68.973	4/4	29	1.100	1.200	1.320	0.317	100/69	21/3	190/0	21/2	280/21	7/2		FC31	4	172.9	66.1	4.7	498
FC34	22.334	68.972	4/4	31	1.042	1.106	1.153	0.403	28/62	21/2	176/24	21/4	272/13	4/2	3						
FC37	22.363	69.000	4/4	43	1.017	1.032	1.050	0.314	37/75	22/7	225/15	22/7	134/2	8/7							
FC38	22.371	68.991	4/4	31	1.025	1.050	1.075	0.323	125/52	14/9	14/16	16/9	273/34	16/5							
FC39	22.358	68.990	5/5	23	1.027	1.067	1.096	0.459	55/87	14/7	200/3	13/9	290/2	9/7	4	FC39[c3]	5	2.5	−60.8	10.5	54
FC42	22.343	68.964	4/3	36	1.012	1.132	1.145	0.826	184/48	23/2	30/40	23/2	299/13	4/0		FC42[c4]	4	2.7	−44.7	8.3	122
FC43	22.344	68.970	5/5	28	1.038	1.124	1.167	0.515	20/23	8/2	169/53	8/4	280/15	4/2	3	FC43[c4]	5	2.3	−46.2	7.5	106
FC45	22.345	68.965	5/5	39	1.034	1.208	1.249	0.692	103/54	29/8	196/2	30/10	288/36	13/6	4	FC45	5	149.8	51.2	7.8	97
FC46	22.349	68.964	4/4	35	1.064	1.228	1.306	0.537	187/68	9/2	32/21	8/2	298/8	5/2	4	FC46[c5]	4	341.4	−55.1	9.5	60
FC47	22.340	68.957	4/4	34	1.038	1.107	1.149	0.452	101/63	8/3	349/11	8/4	254/24	5/2	3 + 4	FC47[c5]	4	339.1	−51.9	11.2	68
FC47B	22.340	68.957	11/9	36	1.071	1.079	1.156	0.041	85/51	9/6	175/0	17/7	266/39	17/5							
FC48	22.335	68.955	4/4	17	1.025	1.077	1.104	0.493	206/13	24/4	87/64	24/5	301/22	5/4							
FC49	22.339	68.950	4/4	39	1.084	1.073	1.162	−0.024	93/77	19/5	353/2	18/18	263/13	18/5	4 + r	FC49	4	174.4	32.2	8.6	68
FC51	22.303	68.927	3/3	39	1.061	1.166	1.236	0.458	284/81	13/2	45/5	12/2	136/8	5/2	2						
FC52	22.315	68.937	5/5	29	1.029	1.072	1.103	0.379	26/25	25/4	249/58	25/7	126/19	7/5		FC52	4	350	−49.7	5.6	158
FC53	22.314	68.951	7/7	25	1.034	1.030	1.064	−0.076	33/2	4/3	124/18	9/4	297/72	9/3	3 + r						
FC54B	22.316	68.948	5/5	31	1.029	1.029	1.058	0.002	50/6	30/8	319/6	29/8	188/81	9/6	2						
FC55	22.326	68.972	6/6	31	1.043	1.092	1.139	0.320	70/61	16/6	175/8	18/4	269/27	10/5							
FC56	22.321	68.971	4/4	36	1.127	1.185	1.336	0.174	69/60	5/4	194/19	5/4	293/23	7/3	3 + 4						
FC57	22.356	68.982	5/5	33	1.059	1.076	1.139	0.012	18/21	12/7	177/68	15/12	286/8	15/6		FC57[c3]	5	3.3	−58.1	6.7	131
FC58	22.352	68.976	4/4	35	1.034	1.204	1.245	0.695	37/1	40/8	130/75	40/5	307/14	8/5		FC58	4	13.0	−55.3	9.0	187
FC59A	22.333	68.967	6/5	46	1.076	1.213	1.304	0.469	83/37	13/3	186/17	8/3	297/48	10/3	3 + 4						
FC59B	22.331	68.968	10/10	47	1.116	1.227	1.369	0.301	338/31	2/2	174/58	3/1	72/7	2/2							
FC60	22.298	68.959	4/4	68	1.041	1.166	1.214	0.572	15/19	42/6	173/69	45/7	283/7	13/4	4						
FC61	22.316	68.959	4/4	25	1.017	1.082	1.101	0.640	275/49	16/4	176/7	18/14	80/40	17/4		FC61	4	186.3	51.4	13.3	57
FC67[b]	22.287	68.941	5/5	57	1.063	1.238	1.316	0.558	31/44	13/5	210/46	21/11	301/1	22/4	4	FC67	4	1.3	−50.7	7.8	139
FC68[b]	22.275	68.930	4/4	50	1.061	1.158	1.228	0.417	210/8	11/3	100/66	11/6	303/22	8/4	3 + 4						
FC76	22.272	68.946	5/5	25	1.042	1.063	1.108	0.165	16/70	65/3	165/17	65/10	258/10	9/2		FC76	4	349.4	−46.4	14.2	45
FC80[b]	22.220	68.939	4/4	28	1.024	1.051	1.076	0.404	166/31	48/16	10/57	50/24	263/11	26/11	1						
FC81[b]	22.226	68.941	3/3	37	1.031	1.060	1.093	0.304	174/27	8/4	8/62	12/8	267/5	13/4	1						
FC82[b]	22.233	68.931	4/4	37	1.027	1.087	1.116	0.499	178/2	16/4	84/69	16/4	269/21	9/2							
FC83[b]	22.237	68.940	3/3	47	1.015	1.034	1.049	0.413	129/83	16/10	349/5	17/4	259/4	12/8							
Mean			**42**	**35**																	

Table 1 (*continued*)

Fortuna Complex

Site	Lat. (°S)	Long. (°W)	N/n	K$_m$ (10^{-3}SI)	Mean AMS parameters				Mean eigenvectors						Mt	Paleomagnetism					
					L	F	P	T	K$_{max}$ Dec/Inc	e/z	K$_{int}$ Dec/Inc	e/z	K$_{min}$ Dec/Inc	e/z		Site	n	Decl	Incl	α$_{95}$	k
Fiesta Granodiorite																					
FC01	22.353	68.962	4/4	26	1.081	1.063	1.149	−0.056	353/32	15/6	203/54	16/6	92/15	9/5							
FC02[a]	22.367	68.967	10/10	0.2	No consistent results											FC02^{low}	10	164.0	52.0	4.2	134
																FC02^{high}	5	350.2	−56.7	13.9	40
FC10B	22.223	68.942	5/5	37	1.020	1.050	1.071	0.44 4	211/45	25/20	339/32	90/23	89/28	90/16							
FC11	22.257	68.915	7/5	30	1.044	1.039	1.085	−0.026	190/10	9/4	66/73	41/7	282/14	41/6							
FC30	22.374	68.962	12/12	26	1.023	1.044	1.068	0.292	38/5	11/3	228/85	13/5	129/1	8/3							
CEF[a]			5/5	9.2	1.135	1.290	1.464	0.336	318/56	15/8	91/24	16/2	191/22	8/5		CEF	4	172	18	11.2	32
Mean			**6**	**30**																	
San Lorenzo Porphyry																					
FC07	22.288	68.965	6/6	19	1.052	1.061	1.116	0.072	69/57	8/2	213/28	8/5	312/16	6/3		FC07	6	346.4	−66.0	10.5	54
FC08	22.283	68.958	5/5	17	1.031	1.097	1.131	0.514	22/76	13/4	200/14	13/4	290/0	5/3							
FC41	22.385	68.971	4/4	16	1.048	1.063	1.113	0.123	217/39	10/3	81/42	12/5	328/24	9/3							
FC50	22.303	68.927	6/6	11	1.094	1.155	1.261	0.256	220/2	17/2	91/86	17/3	310/3	4/2							
FC54A	22.316	68.948	6/6	6	1.036	1.036	1.073	−0.020	192/19	14/6	96/19	14/9	325/62	10/6							
Mean			**5**	**14**												**FPC**	**14**	**173.2**	**53.1**	**5.4**	**55**

Lat. and Long. are site latitude and longitude (geodetic datum PSAD56). N/n is the number of collected samples/number of samples used in statistics. K$_{max}$, K$_{int}$ and K$_{min}$ are mean AMS eigenvectors which represent the maximum, intermediate and minimum susceptibility intensities, respectively. K$_m$ = (K$_{max}$ + K$_{int}$ + K$_{min}$)/3 is the mean magnetic susceptibility (SI units). L is the magnetic lineation (K$_{max}$/K$_{min}$); F is the magnetic foliation (K$_{int}$/K$_{min}$); P is the degree of anisotropy (K$_{max}$/K$_{min}$); T = (lnF − lnL)/(lnF + lnL) is the Jelinek's parameter (Jelinek, 1981); Dec, declination in degrees; Inc, inclination in degrees; e/z are the semiangles of the major and minor axes of the 95% confidence ellipse, respectively, calculated by the bootstrap method. Mt = microtextures according to the classification of Cruden et al. (1999), where 1 denotes magmatic strain, prefull crystallization, 2 denotes submagmatic strain, low melt percent, 3 denotes solid-state strain, high-temperature, 4 denotes solid-state strain, low-temperature (see main text). n is the number of independent samples used to calculate site-mean paleomagnetic vector. Decl and Incl are declination and inclination of site-mean paleomagnetic vector, α$_{95}$ is cone of 95% confidence around the mean vector, k is the *fisherian* dispersion parameter.

c1, c2, c3, c4, and c5 denote neighbor sites which mean paleomagnetic directions were found to be similar and were combined into a single direction (see Section 8.2 in the main text).

FC02^{low} and FC02^{high} indicate low and high temperature component from the site.

Rotation and flattening:

LPPC full R = 20.6° ± 8.9°; F = 1.7° ± 5.7°.

LP north R = 10.7° ± 13.3°; F = −2° ± 9.2°.

LP south R = 26.0° ± 9.9°; F = 3.2° ± 6.5°.

FC R = 1.8° ± 5.8°; F = 5.9° ± 9.2°.

bold highlights mean (average) values.

[a] Not included in the K mean of the unit.

[b] Sites defining a zone of shallower K$_{max}$ in the northern sector of the Antena granodiorite.

remanence to determine the anisotropy of anhysteretic remanence (AARM; e.g. Raposo et al., 2012) in four sites.

Microstructures in these plutonic complexes were explored by petrographic examination of thin sections from samples of 24 sites of the FPC and 28 sites of the LPPC (Table 1). Additionally, polished sections from samples of 12 sites were studied in order to gain insights into oxide mineralogy.

4. Magnetic mineralogy: strong dominance of multidomain (MD) magnetite

Determining the minerals that dominate the magnetic signal is very important when analyzing AMS data. Petrography and rock magnetism indicate that multidomain (MD) magnetite is the mineral that largely dominates the bulk magnetic susceptibility in the studied plutons. Unit-wide average susceptibility yields values of 32.524×10^{-3} SI for the LPPC and $35.474 \, 10^{-3}$ SI for the FPC (Table 1). Overall, most site-mean susceptibilities fall in the range between $20 \, 10^{-3}$ SI and $40 \, 10^{-3}$ SI, and both plutonic units have identical dispersions about the susceptibility grand-mean (~$9.5 \, 10^{-3}$ SI for both the LPPC and FPC). Nevertheless, within site dispersion is higher for the LPPC, suggesting the FPC has a more homogeneous distribution of oxides over short distances. Zonation on the basis of the bulk magnetic susceptibility is not observed in either of these units.

From petrographic observations we determined that the oxide-content ranges from 1 to 3% in volume. Oxides occur as inclusions in the primary minerals or as discrete phases in connection with mafic clots. In general, the titanomagnetite grains show low-degree oxidation textures (Haggerty, 1991) represented by minor ilmenite lamella development, in some cases being entirely homogeneous. Subordinate ilmenite occurs mainly in sandwich textures or in lesser proportion as isolated crystals, and its relative participation in the oxide mineralogy is more important in the LPPC than in the FPC.

The results of remanent coercivity spectra from anhysteretic remanence after application of the pAR procedure show that low-coercivity, Ti-poor titanomagnetite grains dominate the remanent spectra from these samples (Fig. 2a). This agrees with the petrographic observations, supporting the interpretation that a single generation of magnetite dominates the magnetic mineralogy in these rocks.

The development of hysteresis loops and the acquisition of IRM show that J_S remains at a constant value after closing of the hysteresis loops, indicating a negligible contribution of paramagnetic minerals (mafic silicates, ilmenite) in the bulk magnetic susceptibility at room temperature (Fig. 2b). Indeed, the curves indicate strong dominance of ferrimagnetic, low-coercivity minerals; with most data plotting within the MD field of the Day et al. (1977) classification of domain state for titanomagnetites (Fig. 2c).

5. Paleomagnetic results: evidence for differential rigid-body rotation

Bulk magnetic mineralogy of these plutonic units is dominated by magnetite ranging from multidomain (MD) to pseudosingle domain (PSD) size. NRM intensities commonly ranged from 0.05 to 4 A/m. However, some samples showed values on the order of 20 A/m or higher, suggesting they recorded lightning-induced magnetizations. About 55% of the samples showed just a soft remanence (mostly removed at 30 mT), likely of present-day origin, and so were not considered for further study. Most remaining samples carry a high-temperature, high-coercivity component of magnetization. In most of these cases, a softer component of variable magnitude (from a small fraction to more than 50% of NRM) was removed after applying AF between 10 and 30 mT (Fig. 3a), or even higher values in some samples showing evidence for lightning-induced magnetizations (Fig. 3b). In site FC49 this softer component showed a wide unblocking temperature spectrum, up to 540–560 °C (Fig. 3c), largely overlapping the narrower unblocking temperature spectrum of the higher coercivity component, thus making definition of the latter difficult (compare results from companion specimens of sample LF72, Fig. 3a,c). The intensity of this low coercivity component (Fig. 3a,c) indicates that its resistance to thermal demagnetization is not related to lightning induced magnetization but possibly represents the peculiar behavior of some MD magnetite grains described by McClelland et al. (1996). Samples from an abandoned mine southwest of Chuquicamata (site FC2) have a reversed polarity component carried by magnetite plus an additional normal polarity component carried by hematite (Fig. 3d), the latter probably being related with the mineralization at the site.

Paleomagnetic measurements on the Jurassic–Lower Cretaceous host rocks (site SS) revealed samples carrying either or both normal and reversed polarity (Fig. 3e,f). The reversed polarity component unblocks between 400 and 575 °C and can be successfully removed by AF demagnetization, consistent with magnetite as the carrier. This component has the same polarity and a comparable direction with that isolated in the nearby monzodiorite site (site LP62 in Table 1), suggesting that it is a remagnetization related to emplacement of the pluton. In contrast, the high-temperature component is one of normal polarity, nearly antiparallel to the reversed component, and probably both magnetite and hematite carry it. We speculate that this normal polarity component is the younger in these samples, possibly linked to later deuteric processes. Two directions are extracted from this site, one combining reversed polarity component and another combining normal polarity component (SSLP-R and SSLP-N respectively, Table 1).

We interpret that most of the isolated components in these plutonic bodies are thermoremanent magnetizations. The shallow nature of the intrusions suggests that cooling and blocking of remanence at each
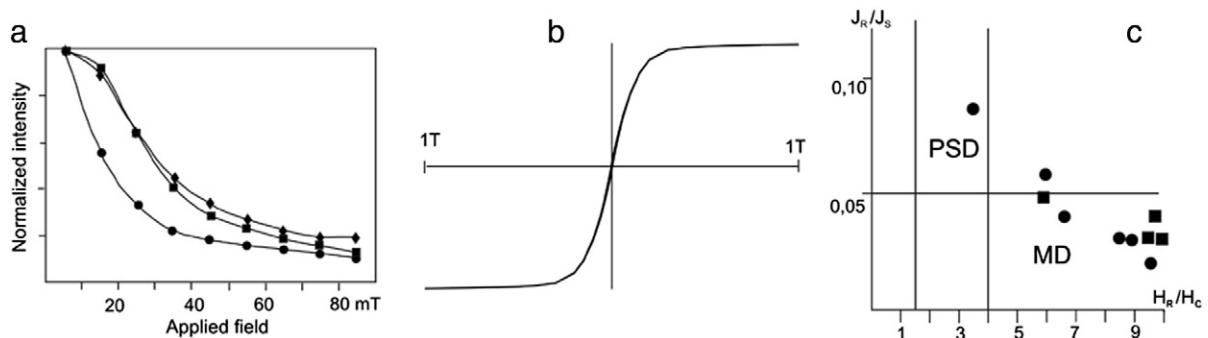

Fig. 2. a) Remanent coercivity spectra from partial anhysteretic remanence for samples from three different sites of the LPPC; b) hysteresis loop for a specimen of the Antena granodiorite; and c) Day et al. (1977) classification of domain state in titanomagnetites, with circle (square) indicating data from the Antena granodiorite (LPPC).
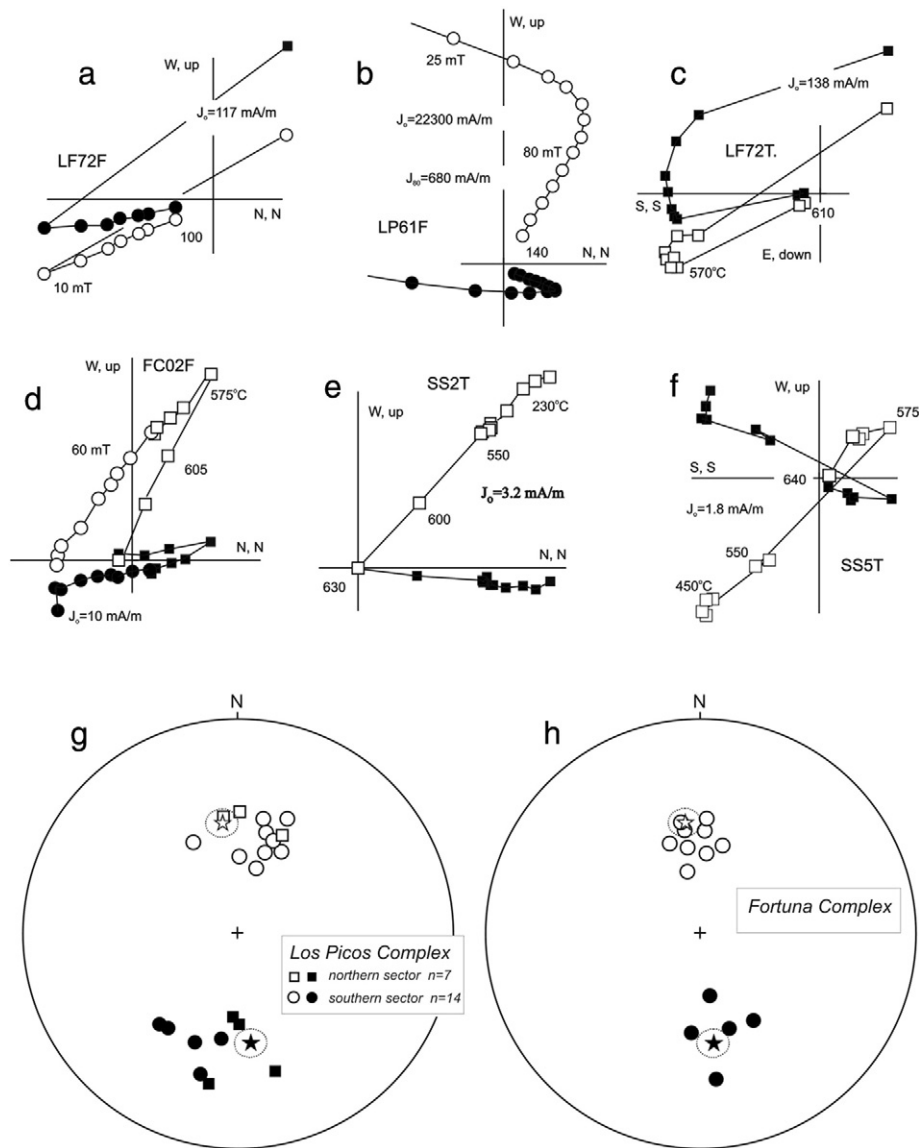
Fig. 3. a to f) Selected examples of paleomagnetic behavior, see main text for description. g, h) Site-mean directions for the LPPC and FPC, white (black) symbols denote normal (reversed) polarities. Stars indicate the position of the reference paleomagnetic field and is shown for both reversed (Decl. 171.4°E; Incl. 47.2°; $\alpha_{95} = 4.8°$; Somoza, 2007) and normal polarity states. Data from LPPC are divided into northern (squares) and southern (circles) sites. R and F values are given at the foot of Table 1.

site did not span a long time-interval, which may also have been the case for the reversed polarity remagnetization in the Jurassic–Lower Cretaceous country rocks of the SS site. The additional components observed in both the latter site and the FC02 site (abandoned mine) are interpreted to be related with hydrothermal activity. Table 1 lists paleomagnetic results from these rocks. We discarded for tectonic interpretation the results from only two independent samples from the site LP72 and the results from site CEF because their corresponding mean direction is separated by more than 2σ from the FPC grand mean.

Most outcrops of both the LPPC and the FPC are continuous with little or no evident internal disruption by brittle faulting. This physical continuity of outcrops would suggest that the major cause of dispersion in paleomagnetic directions within each unit is secular variation of the paleofield (PSV). In fact, both plutonic bodies show normal and reversed polarities (Fig. 3g,h), each unit yielding a positive class "C" reversal test (McFadden and McElhinny, 1990). We conclude that PSV has been averaged out by the results in these plutons, and therefore the time-averaged directions in Table 1 acceptably represent the Eocene magnetic field in outcrop (geographic) coordinates.

Despite LPPC and FPC having similar ages, 45–42 Ma and 39–37 Ma, respectively, their time-averaged paleomagnetic directions are different at the 95% confidence level (LPPC and FPC entries in Table 1, angular separation 12.2° ± 5.7°). Moreover, a closer inspection of the data reveals two things: 1) that most of the paleomagnetic difference between the plutonic complexes resides in the declination of their time-averaged paleomagnetic vectors, the inclinations being statistically indistinguishable (4.2° ± 5.5°) from each other, and each being indistinguishable from the expected inclination for the Eocene paleofield in the area; and 2) that there is a less pronounced but still marginally significant difference in the paleomagnetic record from the northern and southern parts of the LPPC (Fig. 3g; "LPnorth" and "LPsouth" entries in Table 1, angular difference 10.5° ± 9.1°). The discrepancy between the mean paleomagnetic directions of the whole LPPC and the FPC indicates the occurrence of a relative motion between the two plutonic units. Since the FPC is the younger one and it is paleomagnetically concordant with the reference field, it is likely that the LPPC (or at least part of it; see below) has been tectonically disturbed from its original position before the FPC locked its remanence. End member possibilities to account for the

discordant paleomagnetic direction of the LPPC are either about 15° tilt toward the east or between 15 and 20° clockwise vertical-axis rotation. In the section Discussion we argue in favor of the latter case and explore the origin of the intra-LPPC paleomagnetic difference.

6. Microstructures: coexistence of magmatic and solid-state strain

Petrographic observations on samples from 52 sites were made in order to gain insights into the petrofabric in these rocks. Microstructures within the LPPC and the Antena Granodiorite formed under conditions ranging from prefull-crystallization to low-temperature solid-state deformation. We classify the microstructures into four main types following the classification scheme of Cruden et al. (1999).

Fabric type 1 is magmatic, formed under conditions of prefull-crystallization. Grain boundaries are mostly straight and quartz shows only very weak undulose extinction.

Fabric type 2 formed under low melt percent, in the submagmatic state of Paterson et al. (1989) and Bouchez et al. (1992). Quartz grains have moderate undulose extinction, with the formation of some incipient deformation bands, although no changes in the shape of the grains is apparent. Biotite may show some bending and feldspars are not obviously strained although myrmekites develop locally.

Fabric type 3 group characterizes high-temperature solid-state deformation, in the range of ~500 to 700 °C, that is, near-solidus to subsolidus temperatures (Paterson et al., 1998). Main microstructures diagnostic of this type of fabric are chessboard subgrain pattern in quartz (above 700 °C, Blumenfeld et al., 1986; Mainprice et al., 1986), local development of myrmekites (Passchier and Trouw, 2005) and abundant flame perthites in K-feldspar (Pryer, 1993). Other microstructures of this stage are inversion of orthoclase to microcline (Eggleton and Buseck, 1980) and undulose extinction in biotite.

Fabric type 4: is due to strong post-emplacement solid-state deformation, where recrystallization of most minerals into small grains is common, though not complete. Subgrains may be organized in bands. Microstructures include subgrains in quartz and incipient bulging in feldspars, also microfracturing in feldspars. These processes occur at relatively low to medium temperature conditions (300–500 °C) and/or fast strain rates (Passchier and Trouw, 2005; Vernon, 2000). A common characteristic of type 4 fabric is incipient subgrain formation (evidence of dynamic recrystallization) in microcline, which is indicative of temperatures between 450 and 600 °C (Passchier and Trouw, 2005). The fabric subtype 3 + 4 is the combination of fabric 3 with fabric 4, where deformation started in high-temperature conditions (fabric 3) and followed in low-temperature conditions (fabric 4).

In both units solid-state deformation fabrics (3, 4 and 3 + 4) are more abundant than purely magmatic (fabric type 1) and submagmatic ones (fabric type 2). In LPPC fabric ranges from magmatic or submagmatic (Fig. 4a,b), to high and low-temperature solid state deformation (Fig. 4c,d). Interestingly, some undeformed rocks have myrmekites (Fig. 4b), as this microstructure may be of magmatic origin (e.g. Hibbard, 1987) or it may form during solid state deformation (e.g. Vernon, 1991). A few samples show the typical association of high-temperature deformation microstructures, given by myrmekites, microcline instead of orthoclase and chessboard texture in quartz (Fabric type 3, Fig. 4c). When observed, low-temperature solid-state deformation is incipient in most samples from LPPC, as aggregates of small quartz and feldspar subgrains tend to be isolated instead of being interconnected in shear bands and many mineral boundaries remain straight (Fig. 4c,d). Solid-state deformation in LPPC seems to be aided by or related to hydrothermal alteration, as solid-state deformation fabrics 3, 4 and 3 + 4 are present in the samples where mafic minerals are replaced by chlorite, plagioclase is altered to sericite and K-feldspar is replaced by clays; whereas the freshest samples of this unit tend to have magmatic and submagmatic fabrics.

In the Antena Granodiorite, fabrics also range from magmatic and submagmatic (fabric types 1 and 2) to high and low-temperature

deformation (fabrics 3, 4 and 3 + 4). Solid state deformation fabrics are more intense in this unit than in LPPC, as quartz, feldspar, amphibole and biotite subgrains are nearly always organized in thin bands which tend to be interconnected defining a foliation (Fig. 4e). Porphyroclasts of plagioclase and K-feldspar are fractured and may show intracrystalline deformation features such as kink bands and bending (in the case of plagioclase) and microclinization (in the case of K-feldspar, Fig. 4f). Porphyroclasts always show indented grain boundaries (Fig. 4e,f,g). In contrast with LPPC, solid state deformation in the Antena granodiorite does not seem to be related to hydrothermal alteration.

Some samples of Antena Granodiorite register static recrystallization reflected by fairly coarse and equigranular grains of quartz and feldspar which are free of intracrystalline deformation features and which present triple junctions at 120° (Fig. 4h). The static recrystallization process probably post-dates the solid state deformation event.
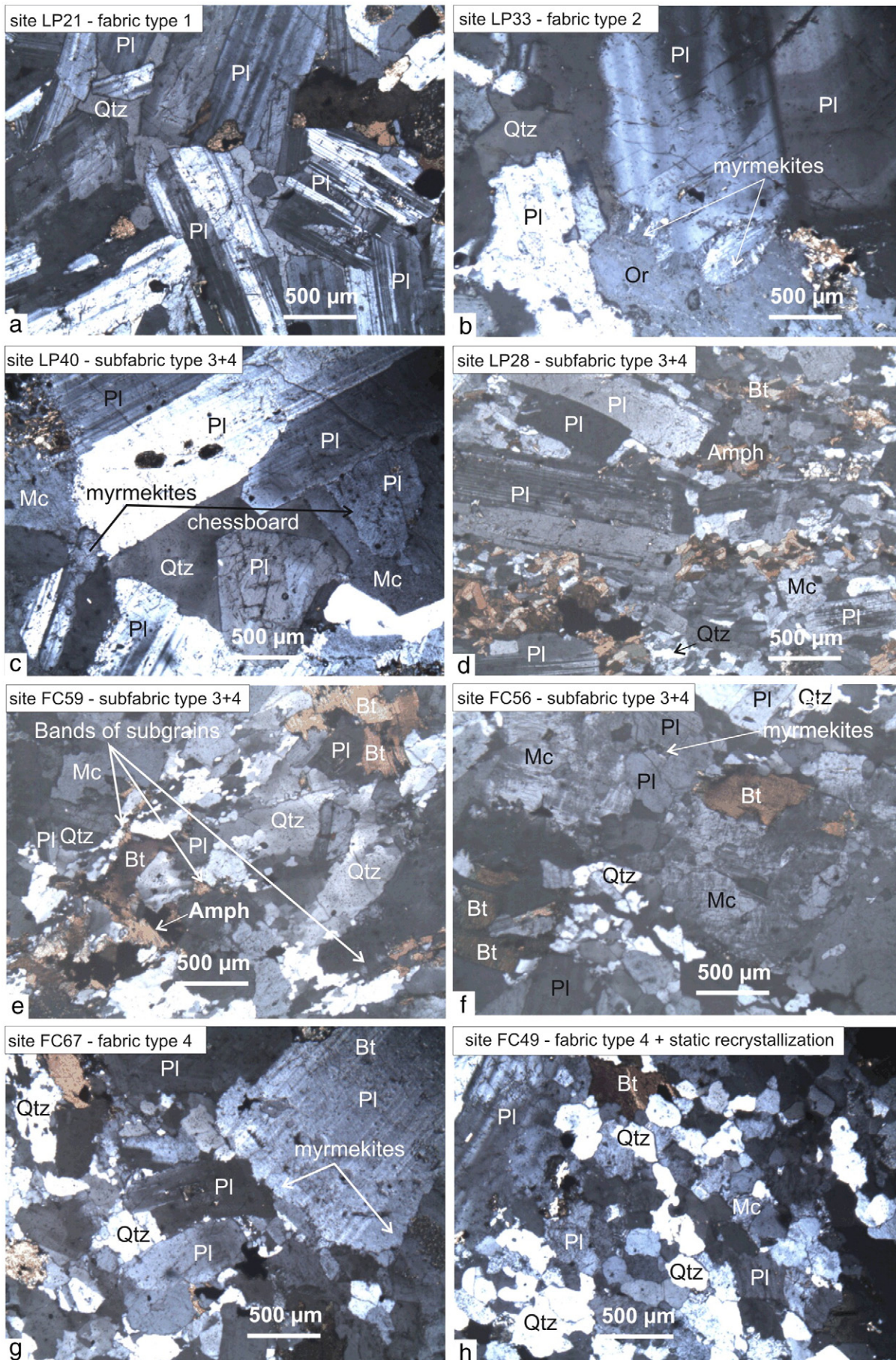
Mylonites are scarce and present only in the FPC, where they appear in isolated N–S to NNE-trending belts at various localities along the length of the complex (Fig. 1c). The southernmost belt, located 3–4 km southwest of Chuquicamata town, was examined and found to be a ca. 600 m wide zone of inhomogeneous deformation consisting of numerous centimetric to metric wide, steeply dipping, mylonitic shears separating wider zones of relatively undeformed granodiorite. The mylonites are formed in medium-grained Antena granodiorite and fine-grained granite aplite dikes. In the granodiorite the shear zones consist of protomylonite at the shear zone margins grading into porphyroclast-rich mylonite in the interiors. Porphyroclasts consist of variably rounded plagioclase and orthoclase with textures indicating both brittle and crystal-plastic behavior, including fractures and microfaults filled with mylonite matrix minerals, undulatory extinction, bent grains and twins, glide twinning, subgrains and weakly to moderately developed, winged, recrystallization mantles. The main mylonitic foliation consists of submillimetric thick alternating layers and lenses of polycrystalline quartz ribbons, very fine grained feldspar-rich layers and biotite-rich ($\pm$ magnetite) layers. Quartz shows static recrystallization with most grains in quartz ribbons being fairly coarse and relatively free of intracrystalline deformation structures. In contrast, feldspar and biotite do not show this strain recovery.

In the granite aplite bodies the shear zones consist of ultramylonite with <1% small orthoclase porphyroclasts in a strongly foliated matrix of submillimetric thick alternating quartz ribbons and fine-grained feldspar-rich layers. The fine-grained nature of the aplite protolith may have contributed to the ultramylonite fabric.

Foliations are N–S to NNE-striking and dip steeply east and west. Mineral lineations are down-dip or steeply plunging. Shear sense was determined in outcrop and oriented thin section by the inclination sense of an oblique S foliation in the protomylonite margins and its curvature sense as it grades into higher strain C-type and C′-type shear bands, the asymmetry sense of sigma-type wings on mantled feldspar porphyroclasts, the asymmetry sense of matrix strain shadows around porphyroclasts, the shear sense of locally well-developed, millimetric scale, C′-type shear bands, and the asymmetry sense of millimetric scale folds in the mylonitic foliation of ultramylonites. Most shear zones examined have a reverse sense-of-movement. Inversion of the kinematic data using a moment tensor summation with uniform weighting of the data (Marrett and Allmendinger, 1990) indicates due E–W directed shortening. We were unable to locate the mylonites with dextral strike–slip shear sense described by Reutter et al. (1996).

7. AMS results: mutually coaxial magnetic fabric and petrofabric

The degree of anisotropy (P) does not show a relationship with the bulk susceptibility (Fig. 5a,b). The LPPC exhibits a rather homogeneous P, with a mean of 1.053 (5.3%); whereas the P for the FPC has a greater dispersion, with sites showing higher values and an overall mean of 1.163 (16.3%). The seven northernmost sites of the Antena granodiorite
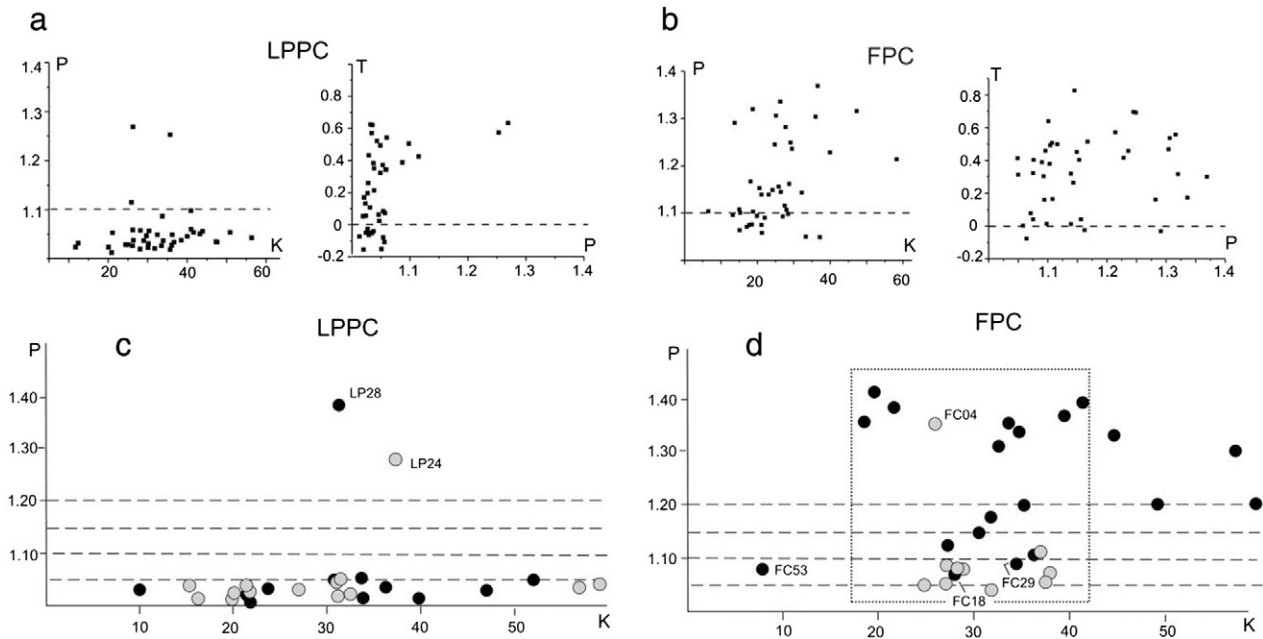
site LP21 - fabric type 1

site LP33 - fabric type 2

site LP40 - subfabric type 3+4

site LP28 - subfabric type 3+4

site FC59 - subfabric type 3+4

site FC56 - subfabric type 3+4

site FC67 - fabric type 4

site FC49 - fabric type 4 + static recrystallization

Fig. 5. a, b) AMS scalar data from LPPC (a) and Antena granodiorite (b), where K is the bulk susceptibility, P is the degree of anisotropy, and T is the shape parameter (Jelinek, 1981), where T > 0 (T < 0) denotes oblate (prolate) ellipsoid. c, d) P vs. K for samples studied by petrography, where gray circles represent magmatic (melt present) fabric, and black circles represent solid-state fabric.

(i.e. those located north of the Chuquicamata mine latitude, see Fig. 8; Table 1) define a sector with relatively lower P values (≤11%). At most sites, the concentration of AMS axes from individual samples define a triaxial ellipsoid, with the planar component being the better developed in most cases, in particular for the Antena granodiorite (Fig. 5a,b). Several AMS ellipsoids from sites in the LPPC show the lineal component better developed than the planar one (Fig. 5a, negative values in the P vs. T diagram). We examined the values from individual samples in these sites, finding that in all cases the distribution of sample directions defines triaxial ellipsoids, and that about half of the individual samples show negative T values. K1 axes tend to be very well clustered in about half of these sites, and in one of them K3 and K2 axes form a girdle, pointing to an intersection origin for the site-lineation.

An interesting relation is found by comparing the type of petrofabric and the magnetic anisotropy. Fig. 5c shows that P in the LPPC is rather constant and independent of the type of petrofabric present. There are two outliers belonging to samples from sites LP24 and LP28, with type 2 and type 3 + 4 fabrics, respectively. In both cases we observed a strong mineral orientation related to magmatic flow, involving euhedral plagioclase megacrysts with straight borders and devoid of intracrystalline deformation. These megacrysts are immersed in a

groundmass composed of mostly undeformed quartz, amphibole, biotite, microcline and plagioclase. The sample from site LP28 (Fig. 4d), however, underwent a mild solid state deformation event (classified as subfabric 3 + 4) which is reflected by incipient microclinization of orthoclase, chessboard extinction in some quartz grains and bulging recrystallization in quartz and feldspars. Thus, these high P values in the samples from the LPPC seem to be associated to strong mineral orientation acquired in the presence of melt (i.e. magmatic fabrics).

In contrast, results from the FPC show a positive correlation between the type of petrofabric and P (Fig. 5d), with solid-state deformation observed in 90% (seventeen out of nineteen) of the samples belonging to sites that plot in the field of P > 1.10; whereas only 27% (three out of eleven) of the samples belonging to sites with P < 1.10 show solid-state strain. One of the exceptions is the sample from site FC04, which shows a sub-magmatic type 2 fabric and high P, the latter is likely due to the strong preferred orientation of plagioclase, amphibole and biotite in this sample. Other exceptions are samples from sites LF18, 29 and 53, which have solid-state deformation and plot in the field P < 1.10 (Fig. 5d). These samples show gentle solid-state deformation where subgrains do not form bands (or very incipient band formation in site LF18), a behavior that resembles the one observed in the LPPC (Fig. 5c).

Fig. 4. Microstructures of Los Picos Monzodiorite (a–d) and of Antena Granodiorite (g–h). a) Magmatic fabric type 1 in a sample from site LP21, where anhedral quartz and amphibole fill the interstices of euhedral plagioclase crystals. Straight mineral borders predominate and quartz is mainly undeformed. b) Submagmatic fabric type 2 in a sample from site LP33 with anhedral orthoclase and quartz and euhedral plagioclase. Curved grain boundaries produced by bulging recrystallization predominate and abundant myrmekitic lobes project on orthoclase. Quartz has undulose extinction. c) A sample from site LP40 with subfabric type 3 + 4 where quartz exhibits chessboard extinction, K-feldspar is microcline instead of orthoclase and myrmekites develop in plagioclase when in contact with microcline. Subgrains in quartz and microcline produced by dynamic recrystallization tend to be organized in bands. d) A sample from site LP28 with subfabric type 3 + 4, this sample has a remarkable foliation produced by magmatic flow due to the strong orientation of euhedral plagioclase crystals. The presence of microcline instead of orthoclase is interpreted as an evidence of superimposition of high temperature solid state deformation. Small recrystallized subgrains (due to low temperature deformation) are observed in quartz and microcline, but they are not organized in bands e) A sample from site FC59 with subfabric type 3 + 4, where low temperature solid-state recrystallization is very strong. Relict quartz grains with chessboard extinction are surrounded by small dynamically recrystallized subgrains devoid of intracrystalline deformation. Microcline is also dynamically recrystallized into small subgrains; quartz and microcline subgrains tend to be organized into shear bands. No straight grain boundaries are observed in the minerals of this sample. f) A sample from site FC56 with subfabric type 3 + 4, where high-temperature solid-state deformation predominates. Microcline grains tend to be fragmented and recrystallized into small subgrains. Local development of myrmekites is observed. g) A sample from site FC67 with fabric type 4. Mineral boundaries are indented by bulging and feldspars are mostly undeformed. Myrmekites are developed in plagioclase in the contact with orthoclase. Quartz crystals have undulose extinction and tend to be surrounded by small recrystallized subgrains. h) A sample from site FC49 with fabric type 4 and the superimposition of static recrystallization. Fairly coarse and equigranular quartz, microcline, plagioclase and biotite grains exhibit frequent triple junctions at 120°. Photomicrograhs were taken with crossed polars and mineral abbreviations in all figures are after Kretz (1983).
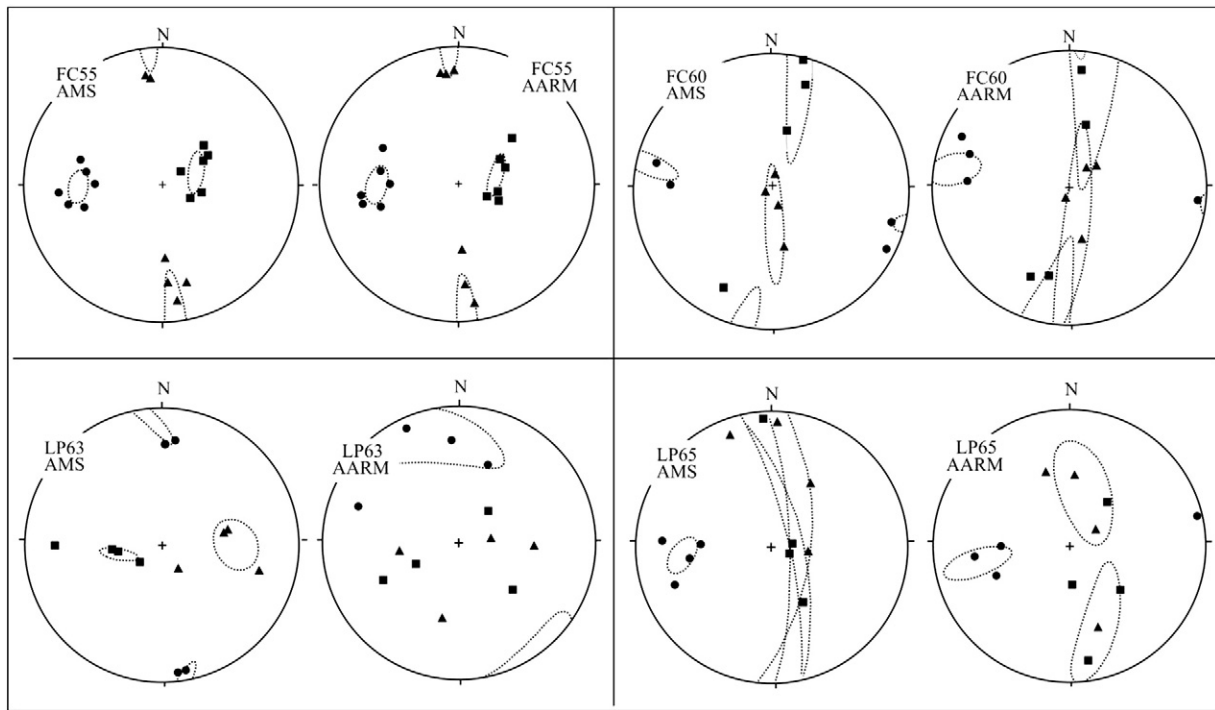
Fig. 6. Comparison of AMS and AARM results for two sites of the Antena granodiorite and two sites of the Los Picos complex. Circles, triangles and squares correspond to minimum, intermediate and maximum axes of each of the ellipsoids represented in the stereograms (lower hemisphere). The AMS and AARM foliations for each site are acceptably coaxial in all the cases. The same is seen for lineations of the Antena granodiorite sites, whereas lineations for the Los Picos complex are less defined. Confidence intervals for maximum and intermediate AARM axes for site LP63 are not shown because they are too large.

Albeit Figs. 5c and d show K and P site-mean values, we have corroborated that individual K and P values from the petrographically studied samples are similar to the corresponding site-mean values. On the other hand, and contrasting with P; the few sites with a negative value for the shape parameter (T; Fig. 5a,b) do not show a tendency to have any particular petrofabric type in the rock (Table 1).

The bulk susceptibility of the studied rocks is controlled by magnetite (Table 1), and the AARM results (Fig. 6) further confirm that magnetite controls the AMS signal. Fig. 5a, b show that the intensity of magnetic anisotropy does not depend on the content of magnetite in the rock. Instead, the results suggest that the strength of solid-state strain in the Antena granodiorite affected the susceptibility signal of magnetite, leading to an increase in the intensity of magnetic anisotropy associated with higher solid-state strain. This behavior could be related to an increase in the shape preferred orientation of individual magnetite grains and/or an increase in the magnetic interactions in clusters of magnetite grains. Previous studies have shown that a preferred orientation of magnetite may be increased by passive rotation of magnetite grains in a deforming matrix (e.g. Mamtani et al., 2011) or by plastic deformation of magnetite grains (e.g. dislocation creep, see Housen et al., 1995). Likewise, increasing the magnetic interactions could be related to subgrain development during solid-state deformation (as observed in quartz and silicates of the studied samples) leading to enhancement of distribution anisotropy (e.g. Grégoire et al., 1995). Further, detailed study is necessary to assess the mechanism for the increase of magnetic anisotropy associated with solid-state deformation in these rocks.

Mean principal susceptibility directions are moderately to well-defined (Table 1). The results show a coherent pattern of moderate to steeply dipping magnetic foliations mostly matching the shape of the plutons (Figs. 7a and 8a), with the Antena granodiorite showing a more organized magnetic fabric than the LPPC. Indeed, foliations in the LPPC are N–S in the southern sector and NW–SE average in the northern sector; with an intervening, short N–S strip of E–W magnetic foliations where rocks have exclusively magmatic fabric and

dominantly prolate magnetic ellipsoids (Fig. 7a; sites LP63, 64 and 86 in Table 1). This allows dividing the unit into two main magnetic domains, which interestingly, roughly correspond with the two sectors showing different paleomagnetic results discussed above (Fig. 3g; Table 1).

Where petrofabric mapping is available, the magnetic foliation attitudes closely match the attitudes of a weak, steeply dipping, mineral foliation of magmatic origin defined by poorly aligned hornblende and plagioclase (Figs. 1c, 6a, 7a; see also Tomlinson et al., 2001). Likewise, the magnetic foliation is also parallel to the mylonitic foliation in the middle part of the FPC (Fig. 8a). Thus the magnetic foliation in the FPC parallels both the magmatic and solid-state structural foliations.

Magnetic lineations show greater spatial variation over short distances than the magnetic foliations. The magnetic lineations from the southern part of the Los Picos complex tend to plunge steeply, whereas both step and shallow lineations are observed in the northern sector (Fig. 7b). The Antena granodiorite displays an interesting pattern of lineations, with zones of steep lineations predominating in the southern part of the body; and shallow, pluton-shape-parallel lineations predominating in its northern part (Fig. 8b).

The parallelism between magnetic and mineral foliations strongly suggests that the magnetic lineation should likewise be parallel to the mineral lineation. This was effectively observed at one site of the Fiesta granodiorite (Fig. 8b). We conclude that the observed magnetic fabric of each of these plutonic units is coaxial with the respective petrofabric. Thus the AMS results complement the mineral foliation data measured in the field and together show a more complete picture of the internal structure of these plutonic units. As we already pointed out, there is no obvious correlation between the type of petrofabric and the directional elements of the magnetic fabric. However, it must be pointed that sites of the Antena granodiorite located north of Chuquicamata mine latitude (those showing P ≤ 1.11, see above) show shallow magnetic inclinations and the microstructures in the three petrographically studied sites from this sector indicate magmatic petrofabric (Table 1;
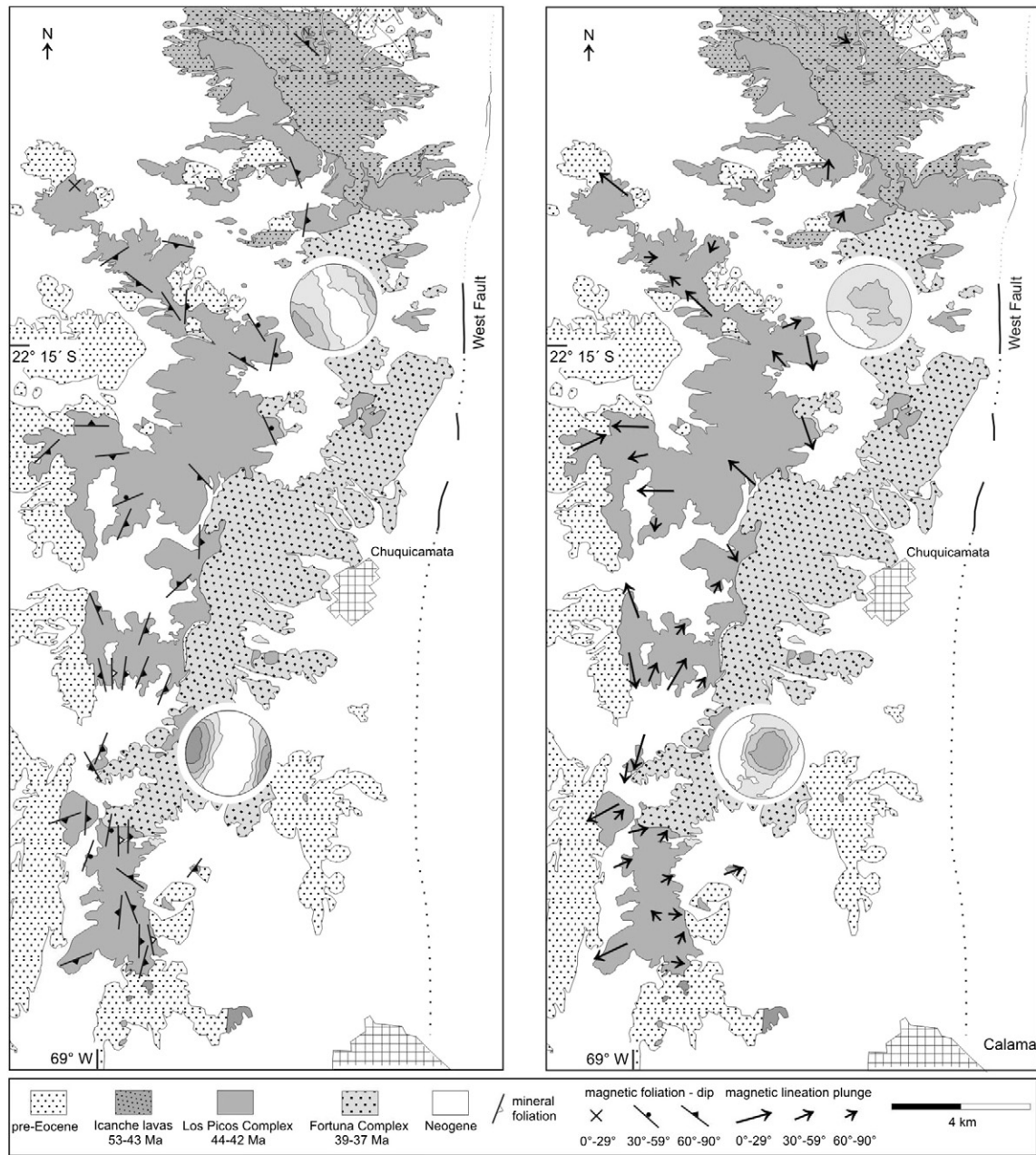
Fig. 7. Observed magnetic foliations (a) and lineations (b) in the LPPC. Kamb density contours (contour interval 2σ) correspond to poles to magnetic foliation and the magnetic lineation for each of two magnetic fabric domains defined by the trend of magnetic foliation and corresponding to the southern and northern parts of the unit (see main text).

Fig. 8a), suggesting that the shallow lineation and relatively low P may be characteristics of a purely magmatic-flow magnetofabric in this unit.

8. Discussion

The paleomagnetic results bear on both the history of tectonic rotations in this part of the Central Andean forearc and provide qualitative information on the time elapsed during the construction of the plutonic bodies. The AMS results show the internal structure of the plutonic bodies and allow exploring their mechanism of emplacement.

8.1. Paleomagnetism: further constraints for the timing of regional tectonic rotations (i.e. CARP) in northern Chile

The paleomagnetic results indicate that the LPPC underwent tectonic motion before the FPC locked its remanence, which may be reconciled

with either about 15° tilt toward the east or 15–20° clockwise vertical-axis rotation. Below we argue in favor of the latter.

Outcrops of the Upper Cretaceous Cerro Empexa Formation, west of the LPPC, persistently show a gentle (4–28°) westward tilt, which is fairly uniform from the northwesternmost exposures of the Los Picos pluton up to a synclinal axis in the Cerros de Montecristo, located ~17 km west of the westernmost outcrops of the LPPC (Fig. 1b; see also Somoza et al., 2012). Thermally metamorphosed Cerro Empexa beds also dip westward at Cerro Negro, on the eastern side of the plutons (Fig. 1c). Although most of this structural attitude probably corresponds to deformation around the Cretaceous-Cenozoic boundary (K–T event; Cornejo et al., 2003; Somoza et al., 2012), we cannot rule out a priori the possibility of a superimposed tilting younger than the LPPC. However, there is no reason to assume that the Upper Cretaceous beds underwent a stronger westward tilt during the K–T event followed by a uniform eastward tilt between 43 Ma (LPPC age) and 39 Ma (FCP
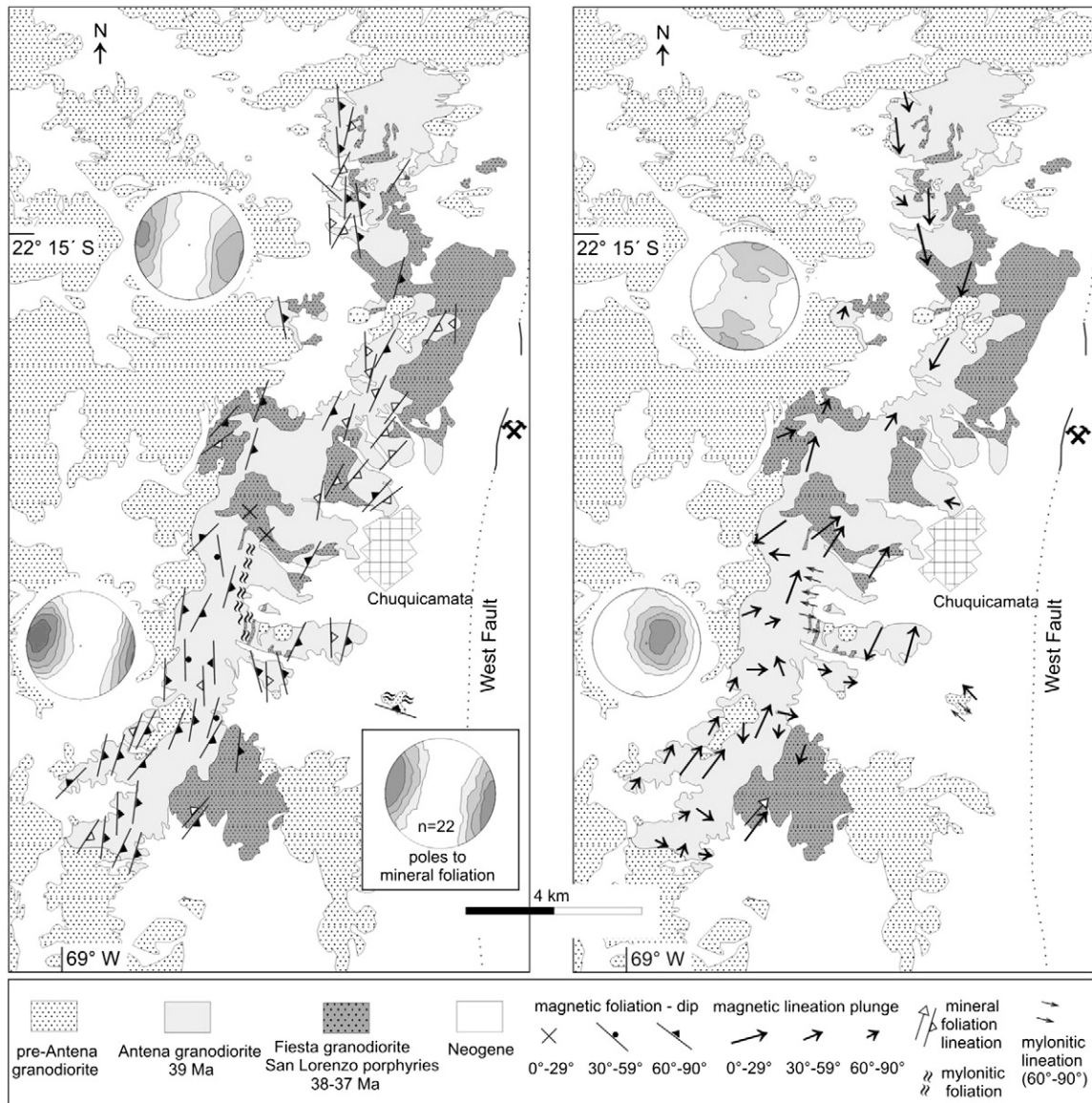
Fig. 8. Observed magnetic foliations (a) and lineations (b) in the FPC. Kamb density contours (contour interval 2σ) in the left side of the figures correspond to poles to magnetic foliation and the magnetic lineation for each of two magnetic fabric domains defined by the plunge of magnetic lineation and corresponding to the southern and northern parts of the unit (see main text). Density contour in the right side of (a) denotes the poles to mineral foliation.

age). In fact, an apatite fission-track study by Maksaev and Zentilli (1999) suggests just the opposite. They interpreted results from a Paleocene quartz monzonite at Cerros de Montecristo (west of the study area; Fig. 1b) to indicate emplacement and rapid cooling at shallow levels with little exhumation (ca. 1.5–2.5 km) since the early Paleocene, whereas results from the FPC indicate exhumation in the Eocene–Oligocene at rates 4–5 times greater, with a total of not more than 2–4 km of exhumation. They relate the higher exhumation rates in the FPC to shortening during the Incaic tectonic phase, suggesting that the exhumation was accomplished by erosion associated with rock uplift. With the exception of the west verging reverse faults near Calama (Fig. 1c), there are no major structural breaks in the Cerro Empexa Formation (Upper Cretaceous beds) across the area, suggesting the Montecristo–Fortuna block forms a single coherent block. Thus, middle Eocene uplift in the FPC and not in the Cerros de Montecristo area would result in westward tilting of the Los Picos pluton. Although Maksaev and Zentilli (1999) do not report data from the Los Picos complex, it seems unreasonable to suggest a radically different Eocene uplift history (e.g.

subsidence) for the post-Los Picos, pre-Fortuna time span, and so it is suggested that any tilting of the LPPC, if it occurred, should have been westward. Any uniform, post-Los Picos westward tilt would mean an even larger clockwise deviation of the declination, after tilt correction, than the in situ mean direction used herein. We conclude that the bulk of the LPPC, and by inference the FPC, did not undergo significant tilting. The fission-track apatite results can be explained by ca. 5° westward tilting, or less, depending on the initial surface topography at the time of exhumation. It is therefore concluded that the paleomagnetic discordance between the LPPC and FPC is related to tectonic rotation of the former before cooling of the later. Rotation and flattening values and their confidence intervals are given at the foot of Table 1.

Another aspect of the paleomagnetic results that need analysis is the slight paleomagnetic difference between the northern and southern sites of the LPPC (Table 1; Fig. 3g). This difference could be ascribed to: 1) the usable paleomagnetic results are not sufficient to fully cancel the paleomagnetic secular variation (PSV) in one or both of these subunits; 2) a differential response to deformation, with the southern

part being more rotated than the northern part; and 3) that the northern outcrops are younger and just record the last increments of the Eocene rotation in the area.

The results do not point to an uncompleted averaging out of PSV in one or both sectors as the cause of the paleomagnetic difference. In a preceding section we have shown that the data define a positive reversal test. Visual inspection of the stereogram (Fig. 3g) corroborates that both subdatasets (southern and northern) have almost antipodal vectors of normal and reversed polarities, which is further supported on statistical grounds, with angular differences between normal and reversed polarity means from the southern and northern sectors being 6.8° ± 9.9° and 6.1° ± 19.4°, respectively. Likewise we discard the second scenario, which ascribes it to a differential rotation within the LPPC, because detailed mapping in the area (Tomlinson et al., 2001) was unable to detect candidate structures necessary to accommodate an intra-LPPC rotation. The third scenario considers the possibility of a younger, syn- to post-rotation age for the northern outcrops, which in this case would have recorded just the last increments of rotation in the area. Although available isotopic ages cannot resolve this possibility, we tentatively favor it, recognizing that more paleomagnetic and particularly isotopic data are necessary to resolve it.

The paleomagnetic results from these intrusive bodies bear on the local timing of regional tectonic rotations. The 45–42 Ma LPPC underwent a clockwise rotation, whereas the 39–37 Ma FPC did not. This indicates that rotation in the monzodiorites likely occurred during the early stage of the Incaic tectonic phase in the area, prior to emplacement and crystallization of the Antena granodiorite, which we interpret as having intruded approximately at mid-stage of the tectonic event. The timing of rotation derived from our paleomagnetic results agree with, and refine the previous constraint of Somoza and Tomlinson (2002); pointing unambiguously that regional tectonic rotations in this part of northern Chile are older than late Eocene. In fact, the results support previous assignations for the bulk of clockwise rotations in northern Chile to the Eocene Incaic orogenic phase (e.g. Arriagada et al., 2000, 2003; Somoza and Tomlinson, 2002).

8.2. Magnetic fabric: pluton formation by episodic injection of magma batches with predominant dyke geometry

Increasingly evidence supports the idea that large, broadly homogeneous upper crustal plutons and batholiths grow through long periods of time by an incremental amalgamation of magma pulses (e.g. Albertz et al., 2005; Coleman et al., 2004; Glazner et al., 2004; Miller et al., 2011; Petford, 1996; Petford et al., 1993, 2000). In agreement with this, our paleomagnetic information indicates that outcrops having remanence of normal polarity are interspersed with those carrying reversed polarity magnetization, unambiguously documenting that both plutonic units formed by multiple episodes of magma injection and cooling through the blocking temperatures. The rather uniform trend of subvertical foliations in the Antena granodiorite strongly suggests that the magma batches that formed this unit mostly emplaced as tabular, subvertical bodies with a NNE mean strike (Fig. 8a). The LPPC also appears to be formed by juxtaposition of predominantly subvertical sheets, although showing, in this case, two separate trends that follow the local map-view shape of the pluton, with a well-defined N–S trend in the southern domain and NW–SE average trend from the more dispersed foliations of the northern domain (Fig. 7a).

The progressive growth of the Antena granodiorite by diking is particularly suggested by cross-pluton paleomagnetic results between Chuquicamata and Cerro Negro (Fig. 1c), where in a ~3 km E–W transect, roughly perpendicular to the subvertical foliations, we detected a N-R-N-R succession of magnetic polarities, illustrating the juxtaposition of magmatic dike-like bodies separated in time. On the other hand, some pairs of neighboring sites share similar paleomagnetic directions (Fig. 1c; see also Table 1). We consider the possibility that the sampled

rocks in these sites representing roughly coeval magma inputs whose derived rocks passed through the blocking temperatures of their oxides at the same time, recording then a similar interval of the secular variation of the paleomagnetic field. These pairs of similar paleomagnetic vectors from neighboring sites have been averaged together (Table 1) in order to avoid the possibility of overestimation of a certain paleomagnetic direction.

Fig. 9a shows that magnetic foliations in sites from the Antena granodiorite having dominantly magmatic (types 1 and 2) fabrics are parallel to the magnetic foliations in sites affected by solid-state strain and are also parallel to the mylonitic foliation observed in outcrop. This, and the greater magnetic anisotropy observed in samples that underwent solid-state deformation (Fig. 5d), suggest that tectonic strain between 700 °C and ~400 °C enhanced, without inducing important directional changes, the original foliation associated to magmatic (melt present) strain (Fig. 9a). This implies that the main petrofabric in this unit evolved under mostly unchanging directional fields from emplacement to progressive cooling, which suggests that emplacement was likely controlled by regional tectonic stress and assisted by structures that were locally active. Nevertheless, the relatively few number of rocks carrying magmatic-only fabric shows a predominance for shallow lineations (7 out of 8 samples, Fig. 9a), suggesting the possibility that this may have been a characteristic in the original magmatic flow pattern within the FPC, as already discussed above. Likewise, solid-state deformation in the FPC shows a tendency to form steep lineations, which are an almost exclusive feature in the mylonites (Fig. 9a).

Contrasting with that observed in the FPC, the magnetic anisotropy of the LPPC does not show a relationship with type of strain (Fig. 5c). As discussed above, one of the differences between these units resides in the nature of low-temperature solid-state strain, which is incipient in the LPPC and well developed in the FPC. This difference may be related either to changing tectonic conditions, with stronger deformation during emplacement of the Antena granodiorite, or to differences in the rheological behavior of the bodies due to differences in composition, water content and solidus temperature. Nevertheless, Fig. 9b shows that magnetic foliations in the southern domain of the LPPC tend to trend N–S for both magmatic and solid-state petrofabric; and likewise, foliations from both types of petrofabric in the northern domain roughly showing a NW–SE average-trend. Then, magmatic and tectonic petrofabrics in the LPPC also show similar orientation for their magnetic foliation, suggesting emplacement and cooling under similar tectonic conditions. As in the case of the Antena granodiorite, we favor that magma emplacement in this unit exploited existing and possibly active structures.

8.3. Tectonic development

The AMS results suggest that the southern sector of the LPPC formed at ca 43 Ma by amalgamation of NW trending, vertical magma sheets (the current N–S trend is after clockwise rotation), with the emplacement spanning at least two paleomagnetic polarity chrons. This southern sector of the LPPC began to rotate sometime after completely blocking the paleomagnetic remanence. Restoring the larger rotation in the southern sector creates a roughly NW–SE trend for the hypothesized feeder conduits/structures at the time of ascent of the magma batches that form the southern LPPC. Our preferred interpretation is that the northern sector of the LPPC was emplaced slightly later, when about half of the finite rotation of the southern LPPC was completed. AMS data suggest that the northern sector was also dominantly formed by juxtaposition of NW trending magma sheets. This northern sector recorded the last increments of the tectonic rotation observed in the LPPC. The magmas of the LPPC were emplaced in an overall contractional environment and likely using pre-existing structures (e.g. Hutton, 1997a, b) which were most probably those associated with the Late
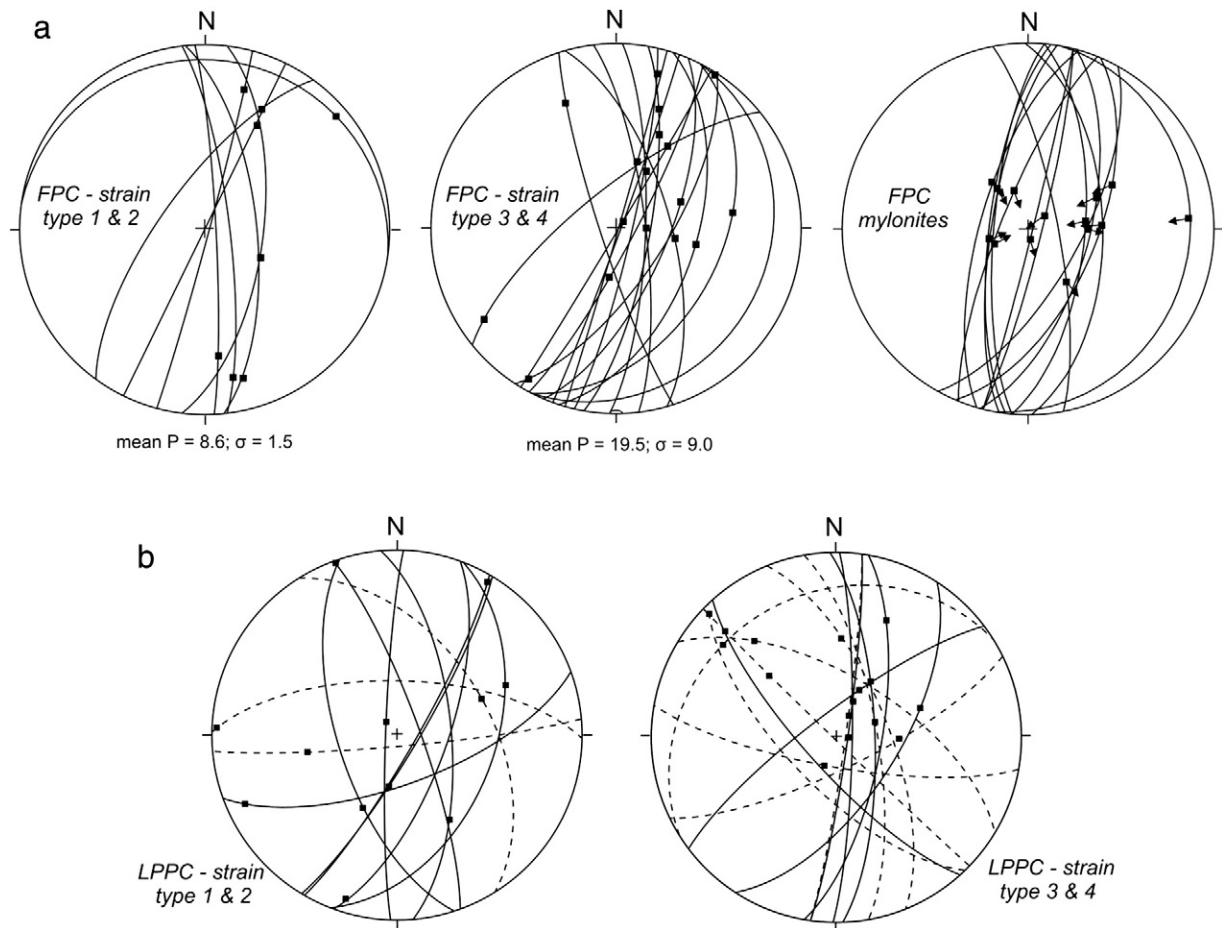
Fig. 9. Directional AMS data from petrographically studied samples and directional petrofabric data from mylonites, showing foliation planes, lineations, and sense of motion of the upper block in the mylonites. a) Magmatic (left), solid-sate (center) and mylonites (right) of the Antena granodiorite. Note the similar attitude of foliations irrespective of the type of deformation. Note also the tendency for shallow lineations in the magmatic only fabrics. b) The same as in (a) for the LPPC. Solid (dashed) planes indicate foliations from the southern (northern) domain of the unit.

Cretaceous thrusting in the studied area, which in turn, in many cases, represent inverted Jurassic–Early Cretaceous extensional faults.

Tectonic rotation of the LPPC was completed by the time of emplacement of the first intrusions of the Antena granodiorite. AMS results suggest that the Antena granodiorite likewise formed by amalgamation of vertical magma sheets. The parallelism between magmatic and solid strain foliations in the Antena granodiorite (Fig. 9a) indicates ascent, emplacement and cooling of successive magma batches under the control of a regional stress field and likely using active structures. The fact that this unit is not rotated, but that the AMS fabrics parallel those in the LPPC implies that the same structural set used for magma ascent in emplacement of the LPPC was used for construction of the FPC but in its new reoriented N–S direction.

In the Oligocene, after complete cooling of the FPC, it began the activity of the West Fault (Fig. 1c) accommodating ~35 km sinistral motion between the forearc and South America (Dilles et al., 1997; Tomlinson et al., 2001), with the associated deformation confined to the narrow fault damage zone (e.g. Astudillo et al., 2008). In the Late Cenozoic the studied area underwent gentle, ~2° westward tilt associated to uplift of the Altiplano.

9. Conclusions

Forty two out of ninety five sites from the Eocene Los Picos and Fortuna plutonic complexes and their host rocks carry high-temperature, high-coercivity magnetizations of likely thermoremanent origin in most of the cases. Magnetite dominates the bulk susceptibility and governs the magnetic fabric of the 93 sites from the plutonic units. Three main conclusions emerge from the tectonic analysis of this study:

1) Paleomagnetic results indicate that the ~43 Ma Los Picos plutonic complex underwent clockwise tectonic rotation, whereas the ~39 Ma Fortuna plutonic complex did not undergo discernible rotation. This, together with previous data from the Miocene Calama Basin (Somoza and Tomlinson, 2002), point to a middle Eocene age for the younger tectonic rotations associated with the CARP in this part of northern Chile.

2) Petrofabrics in these plutonic rocks formed under conditions ranging from purely magmatic (i.e. before full crystallization) to low-temperature solid-state deformation. The magnetic foliations evolved from magmatic to tectonic strain without major directional changes, suggesting that the regional stress field controlled ascent, emplacement and rock deformation during cooling. Solid state deformation enhanced the degree of magnetic anisotropy in the more strained unit (Antena granodiorite of the Fortuna complex).

3) Petrofabric and magnetofabric mapping define a coherent pattern of subvertical foliations paralleling the map-view shape of the plutonic bodies, suggesting that they were dominantly formed by amalgamation of subvertical magma sheets which likely exploited Mesozoic structures, locally reactivated in the Eocene, for their emplacement.

Acknowledgments

References

Albertz, M., Paterson, S.R., Okaya, D., 2005. Fast strain rates during pluton emplacement; magmatically folded leucocratic dikes in aureoles of the Mount Stuart Batholith, Washington, and the Tuolumne Intrusive Suite, California. Geol. Soc. Am. Bull. 117, 450–465.

Arriagada, C., Roperch, P., Mpodozis, C., 2000. Clockwise block rotations along the eastern border of the Cordillera de Domeyko, northern Chile (22°45′–23°30′S). Tectonophysics 326, 153–171.

Arriagada, C., Roperch, P., Mpodozis, C., Dupont-Nivet, G., Cobbold, P.R., Chauvin, A., Cortés, J., 2003. Paleogene clockwise tectonic rotations in the forearc of central Andes, Antofagasta region, northern Chile. J. Geophys. Res. 108 (B1), 2032. http://dx.doi.org/10.1029/2001JB001598.

Astudillo, N., Roperch, P., Townley, B., Arriagada, C., Maksaev, V., 2008. Importance of small-block rotations in damage zones along transcurrent faults. Evidence from the Chuquicamata open pit, Northern Chile. Tectonophysics 450, 1–20.

Blumenfeld, P., Mainprice, D., Bouchez, J.L., 1986. C-slip in quartz from subsolidus deformed granite. Tectonophysics 127, 97–115.

Borradaile, G.J., 1987. Anisotropy of magnetic susceptibility: rock composition versus strain. Tectonophysics 138, 327–329.

Borradaile, G.J., Henry, B., 1997. Tectonic applications of magnetic susceptibility and its anisotropy. Earth-Sci. Rev. 42, 49–93.

Bouchez, J.L., 1997. Granite is never isotropic: an introduction to AMS studies of granite rocks. In: Bouchez, J.L., Hutton, D.H.W., Stephens, W.E. (Eds.), Granite: From Segregation of Melt to Emplacement Fabrics. Kluwer Publishing Co., Dordrecht, pp. 95–112.

Bouchez, J.-P., Dclas, C., Gleizes, G., Nédélec, A., Cuney, M., 1992. Submagmatic microfractures in granites. Geology 20, 35–38.

Callot, P., Sempere, T., Odonnen, F., Robert, E., 2008. Giant submarine collapse of a carbonate platformat the Turonian–Coniacian transition: the Ayabacas Formation, southern Peru. Basin Res. 20, 333–357.

Campbell, I.H., Ballard, J.R., Palin, J.M., Allen, C., Faunes, A., 2006. U–Pb zircon geochronology of granitic rocks from the Chuquicamata-El Abra porphyry copper belt of northern Chile: excimer laser ablation ICP-MS analysis. Econ. Geol. 101, 1327–1344.

Charrier, R., Pinto, L., Rodríguez, M.P., 2007. Tectonostratigraphic evolution of the Andean orogen in Chile. In: Moreno, T., Gibbons, W. (Eds.), The Geology of Chile. The Geological Society of London, pp. 21–114.

Coleman, D.S., Gray, W., Glazner, A.F., 2004. Rethinking the emplacement and evolution of zoned plutons: geochronologic evidence for incremental assembly of the Tuolumne Intrusive Suite, California. Geology 32, 433–436.

Cornejo, P., Matthews, S., Pérez de Arce, C., 2003. The KT compressive deformation event in northern Chile (24e27_ S). X Congreso Geológico Chileno, Extended Abstracts Volume (CD), Concepción.

Cruden, A.R., Tobish, O.T., Launeau, P., 1999. Magnetic fabric evidence for conduit-fed emplacement of a tabular intrusion: Dinkey Creek Pluton, central Sierra Nevada batholith, California. J. Geophys. Res. 104, 10511–10530.

Day, R., Fuller, M., Schmidt, V., 1977. Hysteresis properties of titanomagnetites: grain-size and compositional dependence. Phys. Earth Planet. Inter. 13, 260–267.

Demarest, H., 1983. Error analysis for the determination of tectonic rotation from paleomagnetic data. J. Geophys. Res. 88, 4321–4328.

Dilles, J.H., Tomlinson, A.J., Blanco, N., 1997. El Abra and Fortuna complexes: a porphyry copper batholith sinistrally displaced by the Falla Oeste. 8th Congreso Geológico Chileno 3, pp. 1883–1887.

Dilles, J.H., Tomlinson, M. García and H. Alcota, 2011. The geology of the Fortuna Granodiorite Complex, Chuquicamata district, Northern Chile: relation to porphyry copper deposits. 11th SGA Biennial Meeting, pp. 399–401, Antofagasta, Chile

Eggleton, R.A., Buseck, P.R., 1980. The orthoclase-microcline inversion: a high-resolution transmission electron microscope study and strain analysis. Contrib. Mineral. Petrol. 74, 123–133.

Glazner, A.F., Bartley, J.M., Coleman, D.S., Gray, W., Taylor, R.Z., 2004. Are plutons assembled over millions of years by amalgamation from small magma chambers? GSA Today 14 (4), 4–11.

Grégoire, V., de Saint Blanquat, M., Nédélec, A., Bouchez, J.L., 1995. Shape anisotropy versus magnetic interactions of magnetite grains: experiments and application to AMS in granitic rocks. Geophys. Res. Lett. 22, 2765–2768.

Haggerty, S., 1991. Oxide textures — a mini-atlas. In: Lindsley, D.H. (Ed.), Oxide Minerals: Petrologic and Magnetic Significance. Reviews Mineralogy vol. 25. Mineralogist Society of America, Washington D.C., pp. 129–219.

Hibbard, M.J., 1987. Deformation of incompletely crystallized magma systems: granitic gneisses and their tectonic implications. J. Geol. 95, 543–561.

Hongn, F., del Papa, C., Powell, J., Petrinovic, I., Mon, R., Deraco, V., 2007. Middle Eocene deformation and sedimentation in the Puna–Eastern Cordillera transition (23°–26°S): control by preexisting heterogeneities on the pattern of initial Andean shortening. Geology 35, 271–274.

Housen, B.A., Van der Pluijm, B.A., Essene, R.J., 1995. Plastic behavior of magnetite and high strains obtained from magnetic fabrics in the Parry Sound shear zone, Ontario Grenville Province. J. Struct. Geol. 17, 265–278.

Hutton, D.H.W., 1997a. The "space problem" in the emplacement of granite. Episodes 19, 114–119.

Hutton, D.H.W., 1997b. Syntectonic granites and the principle of effective stress: a general solution to the space problem? In: Bouchez, J.L., Hutton, D.H.W., Stephens, W.E. (Eds.), Granite: From Segregation of Melt to Emplacement Fabrics. Kluwer Publishing Co., Dordrecht, pp. 189–197.

Isacks, B., 1988. Uplift of the central Andean Plateau and bending of the Bolivian orocline. J. Geophys. Res. 93, 3211–3231.

Jackson, M., 1991. Anisotropy of magnetic remanence: a brief review of mineralogical sources, physical origins and geological applications, and comparison with susceptibility anisotropy. Pure Appl. Geophys. 136, 1–28.

Jackson, M., Gruber, W., Marvin, W., Banerjee, S.K., 1988. Partial anhysteretic remanence and its anisotropy applications and grain-size dependence. Geophys. Res. Lett. 15, 440–443.

Jelinek, V., 1981. Characterization of the magnetic fabric of rocks. Tectonophysics 79, 63–67.

Kirschvink, J.L., 1980. The least-squares line and plane and the Analysis of paleomagnetic data. Roy. Astron. Soc. Geophys. J. 62, 699–718.

Kretz, R., 1983. Symbols for rock-forming minerals. Am. Mineral. 68, 277–279.

Lamb, S., Hoke, L., 1997. Origin of the high plateau in the Central Andes, Bolivia, South America. Tectonics 16, 623–649.

Mainprice, D., Bouchez, J.L., Blumenfeld, P., Tubia, J.M., 1986. Dominant c-slip in naturally deformed quartz: implications for drastic plastic softening at high temperature. Geology 14, 819–822.

Maksaev, V., Zentilli, M., 1999. Fission track thermochronology of the Domeyko Cordillera, Chile: metallogenetic implications for Andean porphyry copper metallogenesis. Explor. Min. Geol. 8, 65–89.

Mamani, M., Wörner, G., Sempere, T., 2010. Geochemical variations in igneous rocks of the Central Andean orocline (13°S to 18°S): tracing crustal thickening and magma generation through time and space. Geol. Soc. Am. Bull. 122, 162–182.

Mamtani, M.A., Piazolo, S., Greiling, R.O., Kontny, A., Hrouda, F., 2011. Process of magnetite fabric development during granite deformation. Earth Planet. Sci. Lett. 308, 77–89.

Marrett, R., Allmendinger, R.W., 1990. Kinematic analysis of fault–slip data. J. Struct. Geol. 12, 973–986.

McClelland, E., Muxworthy, A.R., Thomas, R.M., 1996. Magnetic properties of the stable fraction of remanence in large multidomain (MD) magnetite grains: single-domain or MD? Geophys. Res. Lett. 23 (20), 2831–2834.

McFadden, P., McElhinny, M., 1990. Classification of the reversal test in paleomagnetism. Geophys. J. Int. 103, 725–729.

McQarrie, N., Horton, B.K., Zandt, G., Beck, S., DECelles, P.G., 2005. Lithospheric evolution of the Andean fold–thrust belt, Bolivia, and the origin of the central Andean plateau. Tectonophysics 399, 15–37.

McQuarrie, N., 2002. Initial plate geometry, shortening variations, and evolution of the Bolivian orocline. Geology 30, 867–870.

Mégard, F., 1984. The Andean orogenic period and its major structures in central and northern Perú. J. Geol. Soc. Lond. 141, 893–900.

Mégard, F., 1987. Cordilleran Andes and marginal Andes: a review of Andean geology of the Arica elbow (18°S). In: Monger, J.W.H., Francheteau, J. (Eds.), Circum-Pacific Orogenic Belts and Evolution of the Pacific Basin. AGU Geodyn. Ser 18, pp. 71–95.

Miller, C.F., Furbish, D.J., Walker, B.A., Claiborne, L.L., Koteas, G.C., Bleick, H.A., Miller, J.S., 2011. Growth of plutons by incremental emplacement of sheets in crystal-rich host: evidence from Miocene intrusions of the Colorado River region, Nevada, USA. Tectonophysics 500, 65–77.

Mpodozis, C., Ramos, V.A., 1990. The Andes of Chile and Argentina. In: En Ericksen, G.E., Cañas Pinochet, M.T., Reinemud, y J.A. (Eds.), Geology of the Andes and its relation to Hydrocarbon and Mineral Resources. Circumpacific Council for Energy and Mineral Resources, Earth. Sci. Ser. 11, Houston, pp. 59–90.

Passchier, C.W., Trouw, R.A.J., 2005. Microtectonics. 2nd. ed. Springer, Berlin (366 pp.).

Paterson, S.R., Vernon, R.H., Tobish, O.T., 1989. A review of criteria for the identification of magmatic and tectonic foliations in granitoids. J. Struct. Geol. 11, 349–363.

Paterson, S.R., Flower Jr., T.K., Schmidt, K.L., Yoshinobu, A.S., Yuan, E.S., Miller, R.B., 1998. Interpreting magmatic fabric patterns in plutons. Lithos 44, 53–82.

Petford, N., 1996. Dykes or diapirs? Trans. Roy. Soc. Edinb. Earth 87, 105–114.

Petford, N., Kerr, R.C., Lister, J.R., 1993. Dike transport of granitoid magmas. Geology 21, 845–848.

Petford, N., Cruden, A.R., McCaffrey, K.J.W., Vigneresse, J.L., 2000. Granite magma formation, transport and emplacement in the Earth's crust. Nature 408, 669–673.

Pryer, L.L., 1993. Microstructures in feldspars from a major crustal thrust zone: the Grenville Front, Ontario, Canada. J. Struct. Geol. 15, 21–36.

Ramos, V.A., 1999. Plate tectonic setting of the Andean Cordillera. Episodes 22, 183–190.

Ramos, V.A., Aleman, A., 2000. Tectonic evolution of the Andes. In: Cordani, U.G., Milani, E.J., Thomaz Filho, A., Campos, D.A. (Eds.), Tectonic Evolution of South America. 31st. International Geological Congress, Río de Janeiro, pp. 635–685.

Randall, D.E., Taylor, G.K., Grocott, J., 1996. Major crustal rotations in the Andean margin: paleomagnetic results from the Coastal Cordillera of northern Chile. J. Geophys. Res. 101, 11,387–11,400.

Randall, D.E., Tomlinson, A., Taylor, G.K., 2001. Paleomagnetically defined rotations from the Precordillera of northern Chile: evidence of localized in situ fault-controlled rotations. Tectonics 20, 235–254.

Raposo, M.I.B., Pressi, L.F., Janasi, V.A., 2012. Magnetic fabrics and their relationship with the emplacement of the Piracaia pluton, SE Brazil. Int. J. Earth Sci. 101, 773–786.

Reutter, K.J., Scheuber, E., Chong, G., 1996. The Precordilleran fault system of Chuquicamata, northern Chile: evidence for reversals along arc-parallel strike–slip faults. Tectonophysics 259, 213–228.

Roperch, P., Fornari, M., Hérail, G., Parraguez, G.V., 2000. Tectonic rotations within the Bolivian Altiplano: implications for the geodynamic evolution of the central Andes during the late Tertiary. J. Geophys. Res. 105, 795–820.

Roperch, P., Sempere, T., Macedo Sánchez, O., Arriagada, C., Fornari, M., Tapia, C., García, M., Laj, C., 2006. Counterclockwise rotation of late Eocene–Oligocene fore-arc deposits in southern Peru and its significance for Oroclinal bending in the central Andes. Tectonics 25, TC3010. http://dx.doi.org/10.1029/2005TC001882.

Roperch, P., Carlotto, V., Ruffet, G., Fornari, M., 2011. Tectonic rotations and transcurrent deformation south of the Abancay deflection in the Andes of southern Peru. Tectonics 30, TC2010. http://dx.doi.org/10.1029/2010TC002725.

Rousse, S., Gilder, S., Farber, D., McNulty, B., Patriat, P., Torres, V., Sempere, T., 2003. Paleo-magnetic tracking of mountain building in the Peruvian Andes since 10 Ma. Tectonics 22, 1048. http://dx.doi.org/10.1029/2003TC00150.

Somoza, R., 2007. Eocene paleomagnetic pole for South America, northward continental motion in the Cenozoic, opening of Drake Passage and Caribbean convergence. J. Geophys. Res. 112, B03104. http://dx.doi.org/10.1029/ 2006JB004610.

Somoza, R., Tomlinson, A., 2002. Paleomagnetism in the Precordillera of northern Chile (22°30′S): implications for the history of tectonic rotations in the central Andes. Earth Planet. Sci. Lett. 94, 369–381.

Somoza, R., Zaffarana, C.B., 2008. Mid-Cretaceous polar standstill of South America, mo-tion of the Atlantic hotspots and the birth of the Andean cordillera. Earth Planet. Sci. Lett. 271, 267–277.

Somoza, R., Singer, S., Coira, B., 1996. Paleomagnetism of upper Miocene ignimbrites at the Puna: an analysis of vertical-axis rotations in the Central Andes. J. Geophys. Res. 101 (11387–11400), 1996.

Somoza, R., Singer, S., Tomlinson, A., 1999. Paleomagnetic study of upper Miocene rocks from northern Chile: implications for the origin of late Miocene—recent tectonic rotations in the southern central Andes. J. Geophys. Res. 104, 22,923–22,936.

Somoza, R., Tomlinson, A.J., Caffe, P.J., Vilas, J.F., 2012. Paleomagnetic evidence of earliest Paleocene deformation in Calama (22°S), northern Chile: Andean-type or ridge-collision tectonics? J. S. Am. Earth Sci. 37, 208–213.

Taylor, G.K., Grocott, J., Dashwood, B., Gipson, M., Arévalo, C., 2007. Implications for crustal rotation and tectonic evolution in the central Andes fore arc: new paleomagnetic re-sults from the Copiapó region of northern Chile, 26°–28°S. J. Geophys. Res. 112, B01102. http://dx.doi.org/10.1029/2005JB003950.

Tomlinson, A.J., Blanco, N., Maksaev, V., Dilles, J., Grunder, A.L., Ladino, M., 2001. Geología de la Precordillera Andina de Quebrada Blanca e Chuquicamata, Regiones I y II (20_ 300e22_ 300S). Servicio Nacional de Geología y Minería, Informe Registrado IR-01e20, Santiago, Chile (444 pp.).

Tomlinson, A.J.; Blanco, N.; Dilles, J.H. 2010. Carta Calama, Región de Antofagasta. Servicio Nacional de Geología y Minería, Carta Geológica de Chile, Serie Preliminar 8: 3 anexos, escala 1:50.000. Santiago, Chile, 42 pp.

Vernon, R.H., 1991. Questions about myrmekite in deformed rocks. J. Struct. Geol. 13, 979–985.

Vernon, R.H., 2000. Review of microstructural evidence of magmatic and solid-state flow. Elect. Geosci. 5 (2), 1–23.